Hecht, James H.; Alexander, M. Joan; Walterscheid, R. L.; Gelinas, L. J.; Vincent, Robert Alan; MacKinnon, Andrew David; Woithe, Jonathan Mark; May, Peter T.; Skinner, W.; Mlynczak, Martin G.; Russell, J. M.
Imaging of atmospheric gravity waves in the stratosphere and upper mesosphere using satellite and ground-based observations over Australia during the TWPICE campaign, Journal of Geophysical Research, 2009; 114:D18123.

Imaging of atmospheric gravity waves in the stratosphere and upper mesosphere using satellite and ground-based observations over Australia during the TWPICE campaign

J. H. Hecht,[1] M. J. Alexander,[2] R. L. Walterscheid,[1] L. J. Gelinas,[1] R. A. Vincent,[3] A. D. MacKinnon,[3] J. M. Woithe,[3] P. T. May,[4] W. R. Skinner,[5] M. G. Mlynczak,[6] and J. M. Russell III[7]

Received 7 October 2008; revised 20 May 2009; accepted 15 June 2009; published 29 September 2009.

[1] During the Tropical Warm Pool International Cloud Experiment (TWPICE) an intense tropical low was situated between Darwin and Alice Springs, Australia. Observations made on 31 January 2006 by the Atmospheric Infrared Sounder instrument on the NASA Aqua satellite imaged the presence of atmospheric gravity waves (AGWs), at approximately 40 km altitude, with horizontal wavelengths between 200 and 400 km that were originating from the region of the storm. Airglow images obtained from Alice Springs (about 600 km from the center of the low) showed the presence of similar waves with observed periods of 1 to 2 h. The images also revealed the presence of 30- to 45-km-horizontal-wavelength AGWs with shorter observed periods of near 15 to 25 min. Ray tracing calculations show that (1) some of the long wavelength waves traveled on rays, without ducting, to the altitudes where the observations were obtained, and (2) shorter-period waves rapidly reached 85 km altitude at a horizontal distance close to the storm, thus occurring over Alice Springs only if they were trapped or ducted. The mesospheric inversion layer seen in the measured temperature data almost forms such a trapped region. The winds therefore critically control the formation of the trapped region. Wind profiles deduced from the available data show the plausibility for the formation of such a trapped region. Variations in the wind, however, would make ideal trapped region conditions short-lived, and this may account for the sporadic nature of the short-period wave observations.

Citation: Hecht, J. H., et al. (2009), Imaging of atmospheric gravity waves in the stratosphere and upper mesosphere using satellite and ground-based observations over Australia during the TWPICE campaign, *J. Geophys. Res.*, *114*, D18123, doi:10.1029/2008JD011259.

1. Introduction

[2] Although atmospheric gravity waves (AGWs) have been imaged in the airglow for over 30 years [*Hecht*, 2004], their sources have not been fully determined. While convection in the troposphere is likely a major source especially in the tropics [*Fritts and Alexander*, 2003], the nature of the AGWs they produce and how they reach the 80 to 100 km altitudes where airglow originates are still uncertain. It has been particularly difficult for ground-based imaging techniques to study this problem. First, short horizontal wavelength AGWs, often seen in images, typically reach the airglow region only a few hundred kilometers from their source, which means that ground-based imagers need to be placed close to the source region. But periods of intense convective activity are also periods of considerable cloudiness, which often precludes imaging observations. Second, there is some evidence that the AGWs seen in imagers may be ducted a considerable horizontal distance from their source, making it difficult to determine the origin of those waves [e.g., *Walterscheid et al.*, 1999]. Third, until recently, there were almost no space-based instruments capable of imaging AGWs above the troposphere. Nevertheless, there have been several studies which attempted to determine a specific AGW source. They fall into two classes, (1) those that consider AGWs which travel directly from the convective

[1]Space Sciences Department, Aerospace Corporation, Los Angeles, California, USA.
[2]Colorado Research Associates Division, NorthWest Research Associates, Boulder, Colorado, USA.
[3]Department of Physics and Mathematical Physics, University of Adelaide, Adelaide, South Australia, Australia.
[4]Centre for Australian Weather and Climate Research, Melbourne, Victoria, Australia.
[5]Department of Atmospheric, Oceanic and Space Sciences, University of Michigan, Ann Arbor, Michigan, USA.
[6]Climate Science Branch, NASA Langley Research Center, Hampton, Virginia, USA.
[7]Center for Atmospheric Sciences, Hampton University, Hampton, Virginia, USA.

0148-0227/09/2008JD011259

source to the observation altitude and (2) those which consider the ducting or trapping of AGWs.

[3] In the first category, there are to our knowledge only a few such reports. The first was a ground-based study by *Taylor and Hapgood* [1988]. They observed curved wave fronts which they determined had a center about 200 to 500 km from the observed wavefronts. They used estimates of the wind and temperature profiles from the limited satellite and model data then available for their analysis. The observed horizontal wavelength, λ_h, was about 25 km, and the intrinsic period was found to be about 17 min. They concluded that the AGWs took about 6 h to reach airglow altitudes and winds were found to steer the wave packets about 200 km to the west. From meteorological charts and lightning data they showed that there were transient thunderstorms present in the right region to be the source of these AGWs.

[4] A second study was based on space-based observations by *Dewan et al.* [1998]. They used infrared data observed by the Midcourse Space Experiment (MSX) satellite and originating near 40 km altitude which showed circular wavefronts whose λ_h was about 25 km. They followed the analysis procedures used by *Taylor and Hapgood* [1988]. However, since they did not have time resolution, they could only place reasonable limits on the frequency and other derived parameters. For comparison with [*Taylor and Hapgood*, 1988], their intrinsic period was estimated at about 10 min. However, their analysis was convincing that the source was a transient thunderstorm.

[5] A third study was by *Sentman et al.* [2003], who were observing sprites over convective sources. Their viewing geometry allowed them to observe AGWs over thunderstorms, and their airglow images showed nearly concentric wavefronts emanating from a tropospheric source region. Their analysis, which because they had no winds assumed that the observed period was the intrinsic period, showed λ_h values between 40 and 50 km with periods near 10 min. This study is quite impressive in that the link between the convective source and the AGW observations appears well established.

[6] In the second category, there are a number of studies that attempt to explain the prevalence of AGWs in airglow imagers with λ_h values that are typically a few tens of kilometers, have ground-based periods of ten to a few tens of minutes, and are imaged a great distance away from a specific convective source [e.g., *Nakamura et al.*, 1999; *Walterscheid et al.*, 1999; *Hecht et al.*, 2001; *Ejiri et al.*, 2003; *Nakamura et al.*, 2003; *Hecht et al.*, 2004; *Suzuki et al.*, 2004; *Pautet et al.*, 2005]. *Walterscheid et al.* [1999] advanced the idea that this was due to ducting of the AGWs in a thermal duct present in the upper mesosphere and lower thermosphere. *Hecht et al.* [2001] later suggested that modifications of this thermal duct by winds need also be considered and that the waves may be trapped rather than purely ducted. A specific example of such horizontal propagation through such a trapped region was the study performed using observations obtained during the Darwin Area Wave Experiment (DAWEX) [*Hecht et al.*, 2004], which occurred from October to December 2001. *Hecht et al.* [2004] modeled the propagation of AGWs produced by intense convective activity at Darwin (12.5°S, 130.8°E), Australia, to the observation region in the airglow over Alice Springs (23.8°S, 133.9°E) about 1290 km to the south.

[7] Finally, also in the second category, *Vadas et al.* [2009] used ray tracing techniques to identify the source of medium-scale AGWs in Brazil with λ_h values up to 160 km. They provide convincing evidence that the source is convection. However, in some cases the AGWs would reach the airglow altitude region close to the source, and thus additional horizontal transport of the wave packets, presumably via trapping or ducting, would be required for the AGWs to reach the atmosphere above the observing site. Modeled temperature profiles are used for this analysis. This study also provides a quantitative analysis of the energy available in the convective source, as parameterized by the measured convective available potential energy (CAPE), and they show that it is sufficient to excite the observed AGWs.

[8] Both categories of observations suggest that in these cases, short-period, short-horizontal wavelength AGWs are produced by convective activity. This seems to be in line with a number of studies that indicate such waves should be produced by these storms [e.g., *Walterscheid et al.*, 2001; *Alexander et al.*, 2004; *Vadas and Fritts*, 2006]. However, these studies also indicate that AGWs with somewhat longer wavelengths (up to a few hundred kilometers) may also be produced. Furthermore, *Walterscheid et al.* [2001] suggest that acoustic waves with periods of a few minutes may also be present in the region above the storm.

[9] The studies cited above provide data on AGWs which are produced by convective activity and which propagate into the stratosphere and mesosphere. However, our knowledge of these two classes of events is far from complete. First, except for the category one [*Sentman et al.*, 2003] study, the identification of specific sources is only tentative. None of the category one studies had realistic winds and temperatures to constrain a ray trace. In the DAWEX study the source was sufficiently removed from the observations that the AGWs could only reach Alice Springs via trapping or ducting; hence the specific source region was uncertain. Second, all the studies cited were most sensitive to, and only reported on, short λ_h, or, in one case [*Vadas et al.*, 2009], medium λ_h AGWs, and thus the presence or absence of larger-scale waves is unknown. Third, all the studies focused on AGWs produced by transient events. None observed airglow emissions during a large storm. Observations during such an event would allow a determination of whether these storms also produce AGWs that have horizontal wavelengths restricted to below 160 km.

[10] The Tropical Warm Pool International Cloud Experiment (TWPICE) which took place during the first 2 months of 2006 near Darwin was organized to study convective storm activity in the troposphere [*May et al.*, 2008]. Two of the deployed instruments, a meteor radar at Darwin and an airglow imager at Alice Springs, were used for observations of wave activity in the 80 to 100 km region. During TWPICE a very intense tropical low developed in the region between Darwin and Alice Springs. The low was nearly stationary for several days and developed into a tropical cyclone like storm. During some of this period the skies were clear over Alice Springs and in particular, on 31 January 2006, ground-based observations showed frequent small λ_h AGWs in the Alice Springs airglow imager. As described in section 3.3.1, these data also allowed observations of

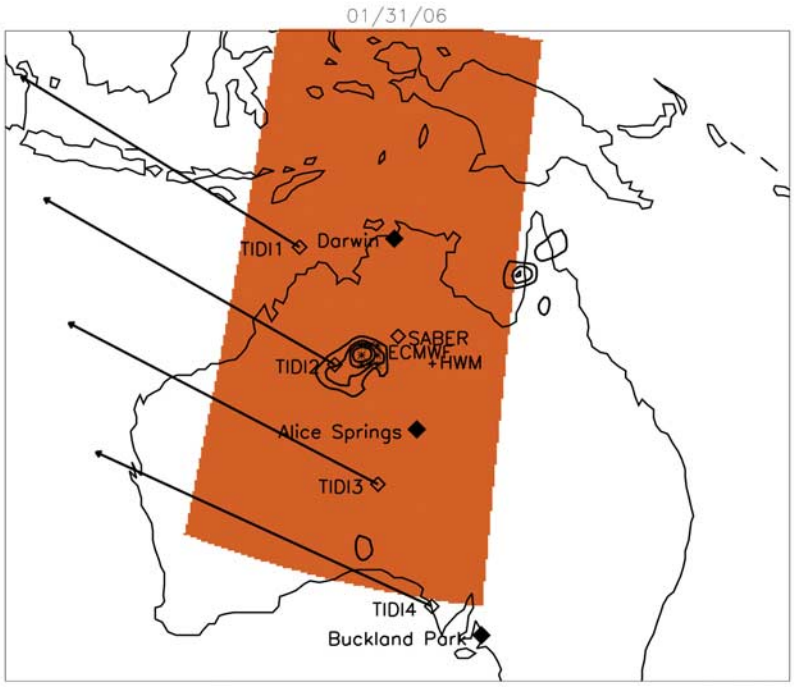

Figure 1. Map of Australia showing the locations of the instruments and models used in this work. The orange represents the extent of the AIRS data swath. The solid diamonds are ground-based sites. The open diamonds are the tangent points of the AIRS and TIMED (TIDI and SABER) satellite observations. The satellite is located off the west coast of Australia moving north to south. Lines are shown from the TIDI tangent points to the satellite location, shown at the end of the arrowhead. The stars enclose the ECMWF grid point. The plus sign shows the location of the HWM profile. See also Table 1. The major rainfall contours over Australia are also shown (see Figure 9).

AGWs whose λ_h are larger than the instrument field of view of about 100 km at airglow altitudes [e.g., *Hecht et al.*, 1997].

[11] In addition to these ground-based observations, there were overpasses of the NASA Thermosphere Ionosphere Mesosphere Energetics and Dynamics (TIMED) and Aqua satellites. Data from the TIMED Doppler Interferometer (TIDI) instrument [*Killeen et al.*, 1999; *Skinner et al.*, 2003; *Niciejewski et al.*, 2006] when combined with the Darwin meteor radar [*Holdsworth et al.*, 2004] and Buckland Park (34.9°S, 138.6°E) medium frequency (MF) radar [*Holdsworth et al.*, 2004] allowed an estimate of the wind fields in the upper mesosphere. These fields could be extended down to the ground using the European Centre for Medium-Range Weather Forecasts (ECMWF) assimilation and Horizontal Wind Model (HWM) [*Hedin et al.*, 1996] data. The TIMED Sounding of the Atmosphere using Broadband Emission Radiometry (SABER) instrument [*Russell et al.*, 1999] allowed temperatures to be determined from the troposphere to above 100 km altitude. Data from the Atmospheric Infrared Sounder (AIRS) instrument [*Aumann et al.*, 2003] on the NASA Aqua satellite are used to image AGWs at approximately 40 km altitude [e.g., *Alexander and Barnet*, 2007; *Alexander and Teitelbaum*, 2007]. This paper reports on these data that provide a means to study AGWs in the upper atmosphere that are generated by this intense tropical storm system.

2. Experimental Instrumentation and Technique

[12] This work uses a number of different ground-based, satellite-based, and model/assimilation techniques. To guide the reader, Figure 1 shows their locations, where applicable. Table 1 lists their main attributes and which parameters they address.

2.1. Data and Models

2.1.1. Airglow Imagers

[13] The airglow instrument at Alice Springs (AS) is a modified version of the Aerospace charge coupled device (CCD) nightglow camera which was originally described by *Hecht et al.* [1994] and further described by *Hecht et al.* [2004]. The imager now uses a 1536 by 1024 Kodak CCD chip. The pixels are binned 8 × 8, resulting in images that have 192 × 128 pixels. The angular field of view is now 46° by 69° giving a spatial field of view of approximately 75 × 122 km at 90 km altitude. This instrument obtains images of the OH Meinel (6, 2) (hereinafter OHM) and O2 Atmospheric (0, 1) band (hereinafter O2A) band emissions. A sequence of five images is obtained, each at 1 min integration, through separate narrow passband filters. Two of the filters cover two different rotational lines of OHM, two filters cover different portions of O2A, and one filter covers the background and has almost no airglow emission in its passband. The latter is used to correct the airglow images for background skylight. Thus one can obtain images of the OHM and O2A airglow, the intensity and temperature of the OHM and O2A emissions, and AGW horizontal wavelengths and ground-based phase velocities [e.g., *Hecht et al.*, 1997, 2001]. The focus in this work is on AGWs so the main discussion will be on OHM image data where the signal to noise is greater.

Table 1. Data Sources[a]

Technique	Type	Location	Lat (°S), Lon (°E)	Time (UT)	Parameter	Altitude (km)	Results
GB	Imager	AS	23.8, 133.9	10–19	Images (OH)	85	AGW λ_h and τ_g
SAT	AIRS	Aqua	Figure 1	16.4	IR(CO_2)	40	AGW λ_h
GB	Meteor radar	DR	12.5, 130.8	Hourly	W	80–100	W 80–100 km
GB	MF radar	BP	34.9, 138.6	Hourly	W	80–100	W 80–98 km
SAT	SABER	TIMED	18.38, 132.55	14.2	T	15–100	T 15–100 km
SAT	TIDI	TIMED	Figure 1	14.2	W	80–100	see section 2.2.2
A	ECMWF	NA	19.5, 130.5	12	W/T	15–50	W/T 15–50
M	HWM/URAP	NA	20, 135	12	W/T	50–84	see section 2.2.2

[a]Lat, latitude; Lon, longitude; GB, ground-based; SAT, satellite; A, assimilation; M, model, AS, Alice Springs; DR, Darwin; W, wind; and T, temperature.

2.1.2. AIRS Instrument on the NASA Aqua Satellite

[14] The NASA Aqua satellite was launched in 2002. One of the instruments on board is the Atmospheric Infrared Sounder (AIRS) [*Aumann et al.*, 2003] that measures IR radiance from many channels including several from the CO_2 15 micron band used in this study. Several of these channels sample high stratospheric altitudes (approximately 40 km) with a vertical weighting function width of about 12 km. These high-altitude channels are insensitive to the influence of tropospheric clouds but would be sensitive to AGWs with vertical wavelengths much above 12 km. The AIRS footprint at nadir is 13.5 km and the image swath is about 1630 km wide. For the high-altitude channels the noise levels are low enough (a few tenths of a degree) so that waves with brightness temperature amplitudes of 1 K can be seen [e.g., *Alexander and Barnet*, 2007; *Alexander and Teitelbaum*, 2007]. The relationship between the measured radiance and derived brightness temperature perturbations is given by equation (5) of *Alexander and Barnet* [2007]. The techniques used to extract AGW amplitudes and wavelengths from these data are wavelet-based and are described in detail by *Alexander and Barnet* [2007]. A main focus of this paper is the observation over central Australia that occurred at approximately 1623 universal time (UT) on 31 January 2006. This swath is shown in orange in Figure 1.

2.1.3. Meteor Radar at Darwin

[15] As part of the TWPICE campaign, a meteor wind measuring radar was located near Darwin. It was an all-sky system similar to that described by *Holdsworth et al.* [2004]. A single crossed-dipole antenna was used for transmission, and five crossed-dipole antennas arranged in a cross configuration were used for reception. Using a 7.5 kW peak power transmitter, about 15,000 meteors were observed each day during TWPICE. This system provided hourly average zonal and meridional winds with a 2-km-height resolution in the 80–100 km height range. Because of the sometimes sparse number of meteor events per hour (as low as 10) and the unpredictable nature of the natural geophysical variability at time scales less than 1 h, an estimate of the uncertainty in the velocity magnitude itself has some error. For this system, in the early morning (2100 UT) when the meteor rates are high (several hundred per hour), the uncertainty is typically about 5 m/s, while in the late afternoon (0800 UT) when the rates are low (20 per hour), the uncertainty can be as high as 20 m/s. At 1400 UT an uncertainty of 10 m/s would be representative.

2.1.4. MF Radar at Buckland Park

[16] An MF radar is located at Buckland Park (BP), some 35 km north of Adelaide, Australia. Operating at 1.98 MHz, it measures winds using the spaced antenna technique in the 60–98 km range by day and 80–98 km range by night. Measurements are made every 2 min at 2-km height intervals. Here we use hourly average zonal and meridional wind components. Further details about the system and techniques used are given by *Holdsworth and Reid* [2004].

2.1.5. SABER Instrument on TIMED

[17] The Sounding of the Atmosphere using Broadband Emission Radiometry (SABER) experiment is one of four instruments on the Thermosphere Ionosphere Mesosphere Energetics and Dynamics (TIMED) satellite [*Russell et al.*, 1999]. SABER scans the atmospheric limb vertically and observes emission in 10 broadband spectral channels. Version 1.07 kinetic temperatures are retrieved from CO_2 15 μm limb emission measurements at approximately 2-km vertical resolution [e.g., *Mertens et al.*, 2001; *Remsberg et al.*, 2008]. The limb tangent points (at 85 km) used below are shown in Figure 1.

2.1.6. TIDI Instrument on TIMED

[18] The TIMED Doppler Interferometer (TIDI) instrument on the TIMED satellite provides profiles of winds in the upper mesosphere and lower thermosphere [*Killeen et al.*, 1999; *Skinner et al.*, 2003; *Niciejewski et al.*, 2006]. The TIDI winds have undergone a recent recalibration, and in this paper, version 10 data are used. We found that only one of the two lines of sight on 31 January 2006 at approximately 1415 UT provided data over nighttime Australia that could be used to track the relative variation of the wind speed from north to south across the continent. This wind direction was approximately 116 degrees east of north, which fortuitously is the closest to the direction of the observed AGWs over Alice Springs described later in this study. Those AGWs propagate at about 150 degrees east of north. The data points are at 2.5-km intervals from 80 to 100 km altitude. At 85 (97.5) km altitude the 1 sigma uncertainty is about 30 (10) m/s. The limb tangent points (at 85 km) used below are shown in Figure 1.

2.1.7. ECMWF

[19] Winds and temperatures up to an altitude of about 50 km were obtained from the output of the operational analysis from the European Centre for Medium-Range Weather Forecasts (ECMWF) assimilation data for 1200 UT on 31 January 2006 [e.g., *Hamilton et al.*, 2004]. The ECMWF data are provided as 1.125 by 1.125 degree grid

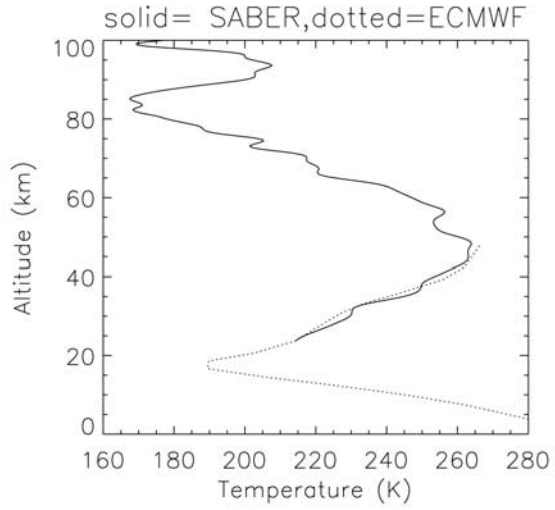

Figure 2. Plot of the adopted temperature profile from SABER (solid curve) and the ECMWF (dotted curve) results. The SABER profile is taken from the overpass on 31 January 2006 at 1413 UT and has a tangent altitude at approximately 18.38° south latitude and 132.55° east longitude. The ECMWF analysis was for 1200 UT at approximately 19.5° south latitude and 130.5° east longitude close to the center of the rainfall seen in Figure 8.

points. Here the point centered at −19.5° south latitude and 130.5° east longitude was used as shown in Figure 1.

2.1.8. HWM/URAP

[20] A major unknown is connecting the ECMWF profile at 50 km with the measured radar wind profiles in the upper mesosphere. Two estimates of winds in this region are available, those from the Horizontal Wind Model (HWM) [*Hedin et al.*, 1996] and those from the Upper Atmosphere Research Satellite (UARS) Reference Atmosphere Project (URAP) [*Swinbank and Ortland*, 2003]. Both are based on climatologies, and the latter is only available for zonal winds. The data used here on 31 January 2006 are from 1200 UT, at −20° south latitude, and 135° east longitude. This location is shown in Figure 1.

2.2. Adopted Winds and Temperatures

[21] In order to analyze the data using analysis techniques described below, temperature and wind profiles were first constructed.

2.2.1. Temperature Profile

[22] Figure 2 shows the temperature profile used for the ray trace analysis that is taken from the SABER overpass on 31 January 2006 at 1413 UT. The adopted profile has a tangent altitude at approximately 18.38° south latitude and 132.55° east longitude as shown in Figure 1. This location is the closest SABER profile in distance (and in time) to the tropical storm that is the presumed source of the observed AGWS and to the ECMWF data used for the winds. For comparison the model temperature profile from ECMWF is also shown. The ECMWF analysis was for 1200 UT at approximately 19.5° south latitude and 130.5° east longitude close to the center of the rainfall discussed below.

2.2.2. Wind Profiles

[23] Here we discuss the derivation of the zonal (U) and meridional (V) wind profiles from 15 to 100 km. These profiles are based partly on data (below 50 and above 84 km) and partly on climatology (between 50 and 84 km). In particular, the meridional and zonal wind profiles up to about 50 km are the ECMWF profiles which, as noted above, are obtained at 1200 UT on 31 January 2006 at a location of 19.5° south latitude 130.5° east longitude.

[24] Above 84 km, available data existed at Darwin and BP. Since the region of interest is south of Darwin and near AS, we produced a wind profile at and above 84 km based on the following considerations. Figure 3 shows measured winds at Darwin and BP at 88 km altitude for the period from 29 January to 2 February 2006 from the meteor and MF radars. Overall the winds are weaker at BP than at Darwin. Since AS is nearly halfway between Darwin and BP, we simply averaged these data sets (from 84 to 98 km) to produce a wind profile to be used for this analysis at and above 84 km. At 100 km we used the Darwin data.

[25] There is a strong quasi 2-day wave (QTDW) at Darwin in the meridional component. The wavelet analysis techniques outlined by *Torrance and Compo* [1998] allow an estimate of the strength of the diurnal tide and the QTDW components. The meridional components at 88 km have amplitudes of approximately 40 m/s for the QDTW and 44 m/s for the tide. The zonal components are weaker, being 12 m/s for the QDTW and 37 m/s for the tide. The uncertainties are about 12 m/s. The QTDW also appears, but much weaker, at BP where the zonal (meridional) component of the QTDW is about 12 (16) m/s with an uncertainty of 15 m/s. The tide appears strongly in the BP data, as it does at Darwin, with both components having amplitudes of between 20 and 25 m/s.

[26] As a further qualitative check on this approximation, Figure 4 shows the TIDI wind profiles for the one line of

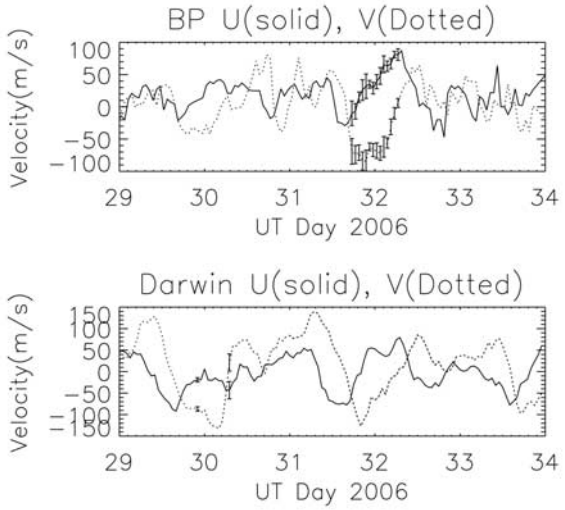

Figure 3. (top) *U* (solid curve) and *V* (dotted curve) components at 88 km altitude from MF radar data at Buckland Park for days 29–33 of 2006. (bottom) Same but from meteor radar at Darwin. Representative error bars are shown.

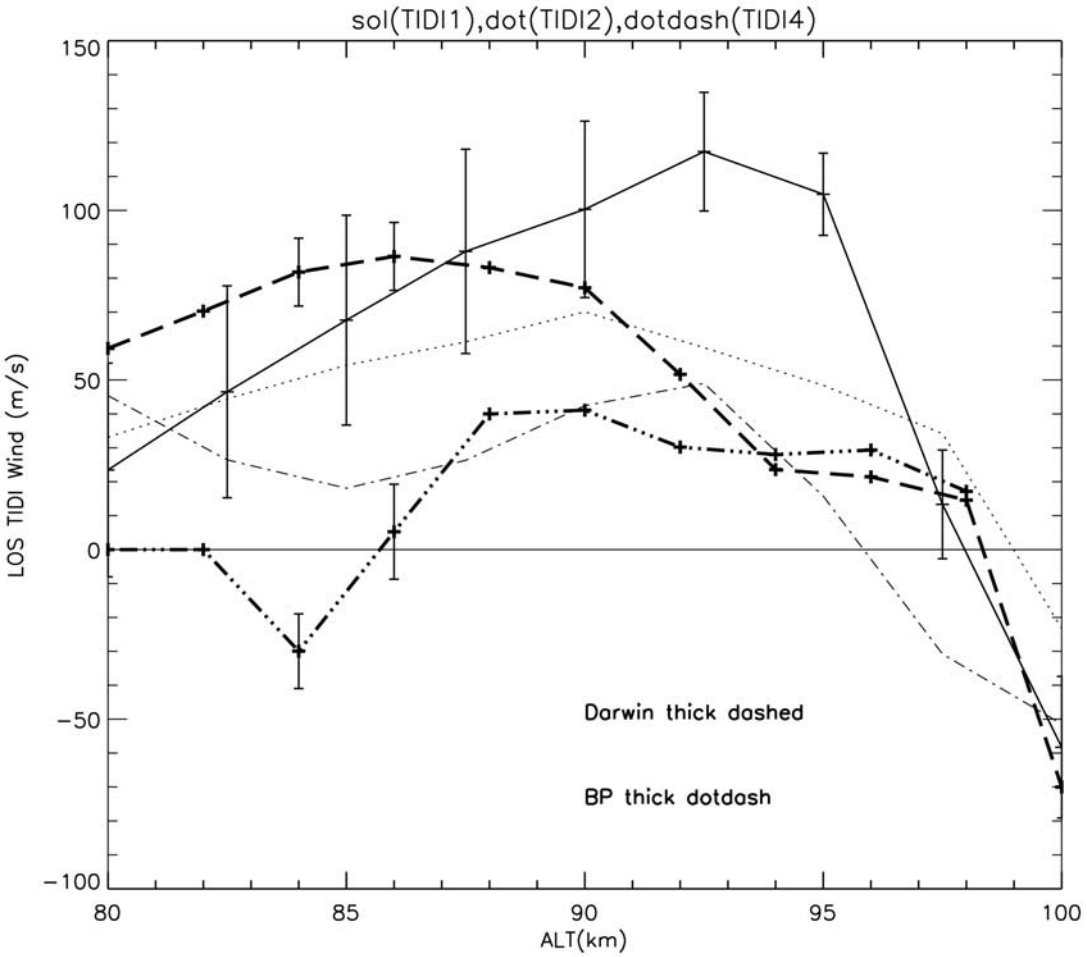

Figure 4. Line of sight (LOS) (approximately 116 degrees east of north) winds from TIDI at about 1415 UT on 31 January 2006 at three positions over central Australia. These positions, TIDI1 (13°S, 125°E), TIDI2 (20°S, 128°E), and TIDI4 (33°S, 135°E), are shown in Figure 1. Also shown are the winds from the BP (35° S, 139° E) and Darwin (12.5° S, 131° E) radars at 1400 UT. A reference line is shown at 0 m/s. Error bars are shown for the TIDI1 plot. The other TIDI errors are similar. For the radar data, representative error bars are shown for two altitudes (84 and 86 km).

sight that was available across Australia at locations shown in Figure 1 at about 1415 UT on 31 January 2006. Also shown are the BP and Darwin profiles at 1400 UT rotated to match the direction of the TIDI line of sight. The TIDI winds and ground-wind data generally overlap considering the error bars, but there are some places where this does not occur, notably between the TIDI1 data and the Darwin data near 93 and 95 km. Note, however, that the TIDI1 tangent point (shown in Figure 1) is west of Darwin by about half an hour in local time. As shown in Figure 3, there can be steep gradients in the wind components, suggesting that a small-phase difference in time could be responsible for this mismatch. Furthermore, the TIDI winds are line of sight winds that smooth out wind variations due to AGWs, while the Darwin radar winds see a different smoothing depending on the distribution of meteor echoes. Also note that the TIDI winds are obtained over a much shorter period of time (seconds) than the Darwin winds, which are averaged over an hour.

[27] Despite these differences in a detailed comparison, it is clear there are many similarities, the most important of which is the change in the magnitude from north to south. Thus our approximation of averaging the Darwin and BP profiles to provide winds in the vicinity of Alice Springs seems reasonable as a first approximation. However, the presence of the strong QTDW, especially at Darwin, does complicate the choice of a characteristic wind to be used above 84 km. In section 3.3.2 where this analysis is further considered we will revisit this portion of the wind profile.

[28] Above 50 km, these need to join the adopted profiles above 84 km, that are based on measured winds at Darwin and BP, with winds in an altitude region where no measured data exist. We used HWM model data, which give results for both zonal and meridional components, for that region. On the basis of these two profiles (ECMWF below 50 km and the adopted radar-based profile above 84 km), we constructed the wind profile from 50 to 84 km based on HWM. We assume a linear interpolation of the winds for both the zonal and meridional components. Figures 5 and 6 show the final adopted profiles and the HWM model results.

[29] We note, however, that the URAP model has a steeper decline in the zonal component from approximately 50 to 65 km than our adopted profile. Given the dynamic effects

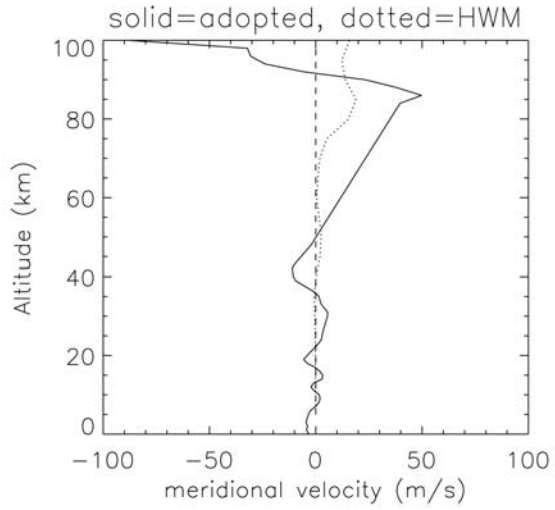

Figure 5. Adopted meridional profile (solid curve) and the closest HWM result at 20°S, 135°E (dotted curve). The dashed line shows 0 m/s velocity to guide the reader.

that can occur above 50 km, the adopted profiles are plausible. However, we will also comment later on the differences that can occur in our analysis if we use the URAP type profile.

2.3. AGW Analysis Techniques

[30] The analysis of AGW intrinsic parameters follows from the dispersion relations shown below [e.g., *Hecht*, 2004]. Consider an AGW at an altitude z above the ground in an atmosphere where H is the density scale height. The vertical wave number, m, is given by $2\pi/\lambda_z$, where λ_z is the vertical wavelength. The vertical wave number obeys the following dispersion relation:

$$m^2 = (2\pi/\lambda_z)^2 = \frac{(N^2-\omega_I^2)(k^2+l^2)}{(\omega_I^2-f^2)} + \frac{\omega_I^2}{c_s^2} - \frac{1}{4H^2} \tag{1a}$$

$$m^2 = \frac{(N^2-\omega_I^2)(k^2+l^2)}{(\omega_I^2-f^2)} + \frac{(\omega_I^2-\omega_a^2)}{c_s^2}. \tag{1b}$$

[31] In equation (1a), c_s is the speed of sound, ω_I is the intrinsic frequency, that is the frequency measured in the frame of reference that moves with the background wind, and f is the inertial frequency which is $2\Omega\sin(\phi)$, where ϕ is latitude and Ω is the angular speed of the Earth. Also, k and l are the vector components of the horizontal wave number, k_h, whose magnitude, $(k^2 + l^2)^{0.5}$, is equal to $2\pi/\lambda_h$. For a given background wind velocity component, $\overline{u}$, in the direction of k_h, and an observed wave horizontal phase velocity, c_o, the intrinsic wave phase velocity, c, is given by $c_o - \overline{u}$ which is equal to ω_I/k_h. The observed (ground-based) period, τ_g, is equal to λ_h divided by c_o. The intrinsic period, τ_I, is equal to λ_h divided by c. In equation (1b) the acoustic cutoff frequency, ω_a, is given by $c_s/(2H)$ in an isothermal atmosphere. Note that when m^2 is negative the AGW is evanescent and it is not freely propagating vertically. Such a region can form a boundary for a trapped or ducted AGW.

[32] We note that the use of the term freely propagating here, and throughout the paper, simply means that m^2 is positive. Such AGWs could still be subject to viscous dissipation and lose energy [e.g., *Gossard and Hooke*, 1975], especially as m becomes large, but such damping is not considered here.

2.3.1. AGW Ray Tracing

[33] Since this work is concerned with possible sources of the AGWs seen in airglow images, it is instructive to incorporate ray-tracing techniques into the analysis. Ray-tracing techniques are used to investigate the effects of background wind and temperature variations on gravity wave propagation. These techniques, as applied to AGW propagation, are well summarized by *Jones* [1969], *Marks and Eckermann* [1995], *Eckermann and Marks* [1996], and *Lighthill* [1978].

[34] For waves with a dispersion relationship G (k, l, m, x, y, z) where (x, y, z) is the position vector, (k, l, m) is the wave number vector, and t is time, the following equations describe the ray path and the refraction of the wave vector along the ray where the time derivatives are following the group motion of the ray packet:

$$dx/dt = \partial G/\partial k, \tag{2a}$$

$$dy/dt = \partial G/\partial l, \tag{2b}$$

$$dz/dt = \partial G/\partial m, \tag{2c}$$

$$dk/dt = -\partial G/\partial x, \tag{3a}$$

$$dl/dt = -\partial G/\partial y, \tag{3b}$$

$$dm/dt = -\partial G/\partial z. \tag{3c}$$

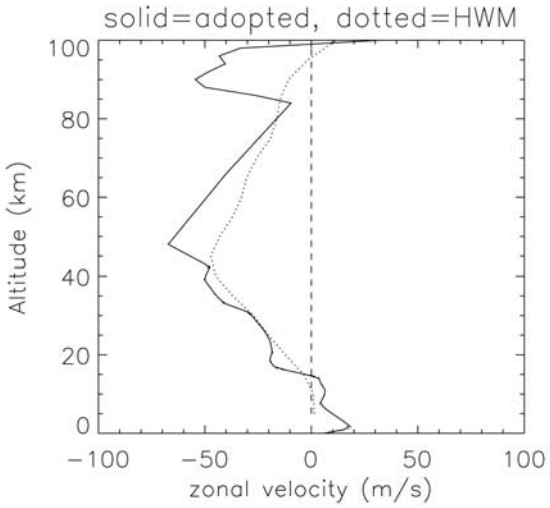

Figure 6. Adopted zonal profile (solid curve) and the closest HWM result at 20°S, 135°E (dotted curve). The dashed line shows 0 m/s velocity to guide the reader.

[35] Equations (2) and (3) show how the ground-based group velocities and the wave vectors are modified by spatially varying winds and temperatures.

[36] Following *Marks and Eckermann* [1995], the nonhydrostatic dispersion relation appropriate for gravity waves on a slowly varying background flow is expressed as

$$\omega_I^2 = (\omega_o - Uk - Vl)^2 \tag{4a}$$

$$\omega_I^2 = \frac{N^2(k^2+l^2) + f^2(m^2 + 1/(4H^2))}{k^2 + l^2 + m^2 + 1/(4H^2)}, \tag{4b}$$

where ω_o is the ground-based frequency. From equation (4) an expression for m, the vertical wave number, follows as

$$m^2 = \frac{(k^2+l^2)\left(N^2 - \omega_I^2\right)}{\omega_I^2 - f^2} - 1/\left(4H^2\right). \tag{5}$$

[37] Equations (4) and (5) differ from equations (1a) and (1b) in that they neglect a term ω_I^2/c_s^2, but for the wave frequencies considered here, this term is negligible. Furthermore, terms including f are also negligible for the wave frequencies considered in this work. Thus, for the AGWs considered here, the difference in m derived from equations (1a), (1b) and (5) can be ignored as it is on the order of 1 percent or less. Equations (4) and (5) can then be used to derive, via equations (2) and (3), the group trajectory of the wave packet through the atmosphere.

[38] For this work, ray tracing was performed with the assumption that the atmospheric wind and temperatures are considered spatially invariant in x and y and time invariant. The resulting equations, which use $\Delta = k^2 + l^2 + m^2 + \alpha^2$, where $\alpha = 1/(4H^2)$, are found in Appendix A of *Marks and Eckermann* [1995]. In equation (6d) the subscript z means taking the spatial derivative of the given quantity with respect to z.

$$dx/dt = U + \frac{k\left(N^2 - \omega_I^2\right)}{\omega_I \Delta}, \tag{6a}$$

$$dy/dt = V + \frac{l\left(N^2 - \omega_I^2\right)}{\omega_I \Delta}, \tag{6b}$$

$$dz/dt = \frac{-m\left(\omega_I^2 - f^2\right)}{\omega_I \Delta}, \tag{6c}$$

$$dm/dt = -kU_z - lV_z - \frac{\left(N_z^2(k^2+l^2) - \alpha_z^2\left(\omega_I^2 - f^2\right)\right)}{2\omega_I \Delta}. \tag{6d}$$

[39] There are several ways to perform a ray trace. We chose to solve these coupled equations using a fourth-order Runge-Kutta algorithm (RK4), as supplied in the Interactive Data Language (IDL) which is based on the algorithms of *Press et al.* [1993]. The wave packet was launched at 15 km altitude (z_0) and at a starting position (x_0, y_0), the location of the storm that generated the AGW. Equation (5) was used to calculate the initial value of m. The group trajectory and wave number were then obtained by numerically integrating, using RK4, equations (2) and (3) with respect to time along the group trajectory, using a time step of 10 s. This procedure allowed the calculation of the distances (δx, δy, δz) traveled in all three spatial dimensions during this 10-s time step. The ray was then relaunched from the new starting position, after recalculating m using equation (5), for another 10 s, and this was continued until the packet reached a given altitude, 40 km for the AIRS data and 85 km for the airglow data, or until m^2 is negative indicating that the AGW is evanescent.

[40] As a practical alternative, we also calculate horizontal and vertical group velocities, using equation (5) to calculate m at the beginning of each interval, and equations (6a), (6b), and (6c) to calculate (δx, δy, δz), varying the time steps so that δz is 1 km. This is done for every altitude in 1-km intervals from 15 km where a wave packet is launched. This is repeated until either the packet reaches a given altitude noted above, or until m^2 is negative indicating that the AGW is evanescent. In this approach it is assumed than m is constant over each altitude step, but as this is an approximation, an error is induced. However, this error is small as long as the variation of m is small.

[41] For the analysis in this work the difference between the two approaches is small (a few percent). Most of the results were calculated using the RK4 method. The alternative method was used, however, for the calculations of trapped AGWs above 85 km which are discussed next.

2.3.2. Trapped AGWs

[42] Some of the AGWs considered here reach 85 km altitude rapidly, in under an hour, traveling only a short distance horizontally from the storm center still many hundreds of kilometers from Alice Springs. However, in certain launch directions, an AGW can encounter an evanescent region between 65 to 80 km a few kilometers thick. If there also exists an evanescent region just above the airglow layer (say 100 km), then a trapped region exists. In an ideal case where the vertical wavelength of the wave is some multiple of the vertical distance of the trapped region, a duct can exist.

[43] The problem of how to treat the propagation of trapped or ducted AGWs in the mesopause region is of some significance. Here we equate trapping with the generic reflection of waves between an upper and lower boundary while a duct includes only those few trapped modes that are resonant. This has generated considerable interest in recent years since *Walterscheid et al.* [1999] suggested that many of the waves seen in ground-based airglow imagers may be ducted, perhaps by a thermal duct that often occurs because of the nominal temperature structure of the 80–140 km region. *Snively and Pasko* [2008] is a recent work that discusses the ducting problem in this altitude region, and many useful references are cited.

[44] There are at least two potential problems with hypothesizing ducted AGWs in the mesopause region. First, because of the large variability, spatially and temporally, of mesopause winds and temperatures, due to the presence of large-amplitude waves and tides, the duct properties could change considerably. Thus it is difficult to see how a perfectly ducted wave would exist for a long (multihour) period. Second, how does a wave enter the duct? If it is easy to enter, then the duct is leaky, while a rigid duct would cause too much wave energy to be lost on entry.

[45] *Hecht et al.* [2001] tried to address these concerns by assuming that instead of a duct the AGW was trapped by regions below and above the airglow layer. In this model a wave passes through the lower evanescent region losing some energy. The wave packet then freely propagates vertically and horizontally until it reaches the upper evanescent region. The wave is then reflected down, losing some energy, and propagates until it reaches the lower region where it is reflected again losing some energy. For different thicknesses of evanescent regions, that were typical of what AGWs seen in airglow imagers might encounter, *Hecht et al.* [2001] calculated how far such an AGW would propagate horizontally until its amplitude was about 10 percent of the original amplitude. In such a case and assuming the original amplitude would produce a few percent density (or airglow temperature) perturbation, the resultant trapped wave would then produce a temperature perturbation of a few tenths of a percent. However, because the perturbation of the airglow intensity amplitude is 5 to 10 times the airglow temperature amplitude, such AGWs would still be visible in airglow images. It was estimated that such AGWs might be able to propagate 1000 km or so. While this model was quite simple, it did show that even if the trapped region did not allow for the formation of a perfectly ducted standing wave, it was possible for AGWs to propagate horizontally a considerable distance away from the source. The trapped region would also select out certain vertical wavelength waves since those would preferentially have the highest amplitudes after traveling a given horizontal distance. Furthermore, as long as there existed a trapped region below, there probably always existed a trapped region above 100 km (nominally around 105 km) due to the large winds that seem to exist almost continuously at the base of the thermosphere [*Larsen*, 2002].

[46] We use here the same simplified approach that was performed by *Hecht et al.* [2001, 2004]. Once the wave packet reached 85 km the wave was assumed to be trapped between layers of evanescence. In the trapped region the wave packets are assumed to be freely propagating, bouncing back and forth between layers of evanescence. We use the alternate ray trace approach to calculate the time it takes for the AGW to propagate vertically between two fixed altitudes that are between the bottom and top evanescent regions. (However, as we note later, because of uncertainties in the available winds, we restrict the region of vertical propagation to that where measured winds are available.) We also calculate the horizontal distance, with respect to the ground, that is traveled during this period. This is then used to calculate how far the wave packet travels (and how many bounces occur) over some multiple of this period. Thus we can estimate, given an initial propagation direction, the location of the AGW after a given amount of time. We note though that although this simplified approach ignores the effects of winds at the boundaries where the waves are evanescent, these effects should be small, since the packet spends most of the time in the free propagation region.

[47] This, however, also ignores the time it takes for the AGW to traverse the evanescent region to reach 85 km. This time can be estimated as follows. While the group velocity in the evanescent region is undefined following *Walterscheid and Hecht* [2003], one can define an energy flow velocity in the vertical as $U_f = F/E$, where F is the wave energy flux and E is the wave energy density. U_f is equal to the vertical group velocity, w_g, just below the base of the evanescent region. To estimate U_f for the evanescent layer, we set $F = TF_o$, where F_o is the incident flux and T is the transmission coefficient for the layer; for an infinite evanescent layer $T = 0$, but otherwise it is nonzero. Thus $U_f = Tw_g$ where T can be calculated following *Hecht et al.* [2001]. *Walterscheid and Hecht* [2003] also give formulas for the horizontal group velocity in the evanescent region. While these strictly only apply to isothermal atmospheres, we apply these to our nonisothermal atmosphere to estimate horizontal propagation since for the parameters considered, N is still much greater than ω_a.

3. Results

3.1. Overview

[48] In this study we concentrate on a period during which a strong isolated tropospheric rainfall source was present and determine whether AGWs could be identified in both the ground-based imager data and the AIRS data. The period we chose to investigate was from 28 to 31 January 2006 with a location over northern Australia. The reason for choosing these dates is that the Tropical Warm Pool International Cloud Experiment (TWPICE) [*May et al.*, 2008] occurred during this period. This experiment was designed to study, in detail, the evolution of tropical cloud systems over northern Australia during a period when large monsoon events are known to occur. In late January 2006 a large tropical low came onshore. In their TWPICE overview paper, *May et al.* [2008] describe this as an event that would have become a tropical cyclone over water had it remained offshore. Instead it established itself as an almost stationary low with a well-defined tropical cyclone like cloud field over land between AS (Alice Springs) and Darwin for several days (26 January to 1 February 2006) causing extensive flooding. This low continued to intensify as it moved inland and formed a well-defined tropical cyclone-like cloud field. The lowest surface pressure recorded from this event was 988 hPa on 31 January 2006. During its intensification it contained a number of well-defined convective bursts as seen from significant areas of cloud. These clouds had brightness temperatures, obtained from the Japanese geostationary satellite MTSAT-IR [e.g., *May et al.*, 2008], that were similar to or colder than the tropopause temperature. This low was also associated with considerable convective and stratiform rainfall. While soundings are not available in the area of the storm, the CAPE that was recorded as the low passed through Darwin on 24–25 January 2006 was above 2000 J/kg [*May et al.*, 2008], indicating the potential for significant strong updrafts. The cloud field associated with the low exhibited many of the characteristics of a developing tropical cyclone, and these often contain significant updrafts even in the absence of high values of CAPE.

[49] Another technique to establish the potential for convective activity is to look at cloud top temperatures also obtained from MTSAT-IR [e.g., *May et al.*, 2008]. Figure 7 highlights the larger and relatively constant coverage of clouds with brightness temperatures (T_B) warmer than about 220 K, and the increases in deep convective activity with T_B colder than the tropopause cold point (approximately 190 K), indicating overshooting cloud tops. This deep convection maximized between about 1200 UT (2130 local time) and

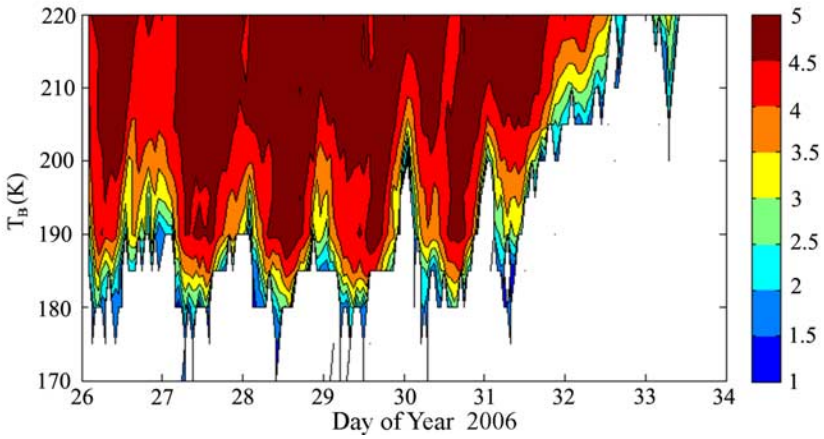

Figure 7. Contours, in intervals of 0.5, of the $\log_{10}$ of the area in km^2 (between 15° to 23° south latitude and 125° to 135° east longitude) covered by cloud top IR brightness temperatures (T_B) as a function of time. Tick marks correspond to 0000 UT of the day of the year in 2006. The plotted T_B values includes data from ±2.5 K from the nominal T_B.

1500 UT each day during the intensification of the storm system. There was a rapid decay in the deep convection after about 1200 UT on 31 January 2006, although heavy rain persisted for about another day.

[50] Figure 8 shows a 24-h rainfall map issued for six periods. Two of the periods, the first and last, are for comparison with the tropical low plots. The first is on 19 January 2006 which shows strong monsoon rainfall typical of the early part of the TWPICE experiment with widespread oceanic convection. Oceanic convection is typically characterized by modest updraft strength [e.g., *Keenan and Carbone*, 1992]. The period on 4 February 2006 shows minimal convective activity.

[51] The other four plots show the period of the tropical low from 28 to 31 January 2006 UT. Note that because of the lack of data the rainfall in central Western Australia, typically in the region between 120° and 130° east longitude and 20° to 30° south latitude, is often not reported. There are three significant regions of rainfall during this period. The most intense is that associated with the tropical low that was northwest of AS. While there is significant rainfall due to the low on 28 January 2006, the rainfall intensified over a small region over the next few days. The most intense rainfall sampled by the rain gauge network occurred on 31 January 2006 when almost 250 mm of rain fell northwest of AS, although it is likely a significant fraction of the rain was stratiform in origin [e.g., *Houze*, 1993]. By this time the cloud structure of the storm system was similar to a tropical cyclone. Note that the upper-level outflow regions of such storms are close to inertially neutral and may also be a source of gravity waves [*May et al.*, 1994] in addition to the direct convective sources indicated by the very cold cloud tops. Thus this is an ideal isolated rainfall event to study with respect to AGW generation.

[52] Note that the maps show that even though most of the rainfall was northwest of AS, there were still patches of rain east of the low. A second region of rainfall was on the Cape York Peninsula in the extreme northeast portion of Australia. As this is the wet season, monsoon rain falls nearly continuously at some locations across northern Australia. However, a statistical study of AGWs has shown that at least with respect to airglow images, few AGWs seem to originate from the east and propagate to the west [*Walterscheid et al.*, 1999]. The third region of rainfall appears associated with a band of rainfall that is moving from the western coast eastward across mainly the central and southern part of the continent. This occurred from 29 to 31 January 2006. On 28 January, there is also considerable rainfall along the northwestern coast. Since the most intense isolated rainfall occurred on 31 January, and there were also good data available from the ground station at AS, most of the analysis will concentrate on that day. However, some comments will also be made about data from the other days.

3.2. AIRS Results

[53] The AIRS data are L1b radiances in mW/m^2-sr-cm^{-1} that can be converted into brightness temperatures [e.g., *Alexander and Barnet*, 2007; *Alexander and Teitelbaum*, 2007]. To identify AGWs, these radiance maps must be analyzed to look for deviations from the mean. The channel we have chosen is in the narrow CO_2 band centered at 667.8 cm^{-1} that has a broad vertical weighting function of nearly 12 km width, and that peaks near 40 km altitude.

[54] Figure 9 shows maps of these radiance perturbations, from three dates (19 January, 31 January, and 4 February 2006) of Figure 8, with an overlay of the largest rainfall contours. Note that the colorbar levels only apply within the image swath. The one-sigma noise level is 0.24 mW/m^2-sr-cm^{-1}. Figure 9 (top) from 19 January 2006 shows intense curved perturbations that may be associated with an AGW radiated from the monsoon rainfall over northern central Australia. Figure 9 (middle) from 31 January clearly shows strong perturbations, exceeding the three-sigma noise level, centered to the northwest of Alice Springs near the largest rainfall contours of the tropical low. The region of largest negative perturbation appears just to the west of the rainfall event contours. Most of the perturbations appear to be symmetric around this region. Figure 9 (bottom) from 4 February 2006 shows little evidence of intense perturbations, consistent with low rainfall on this date. Most of the rest of the

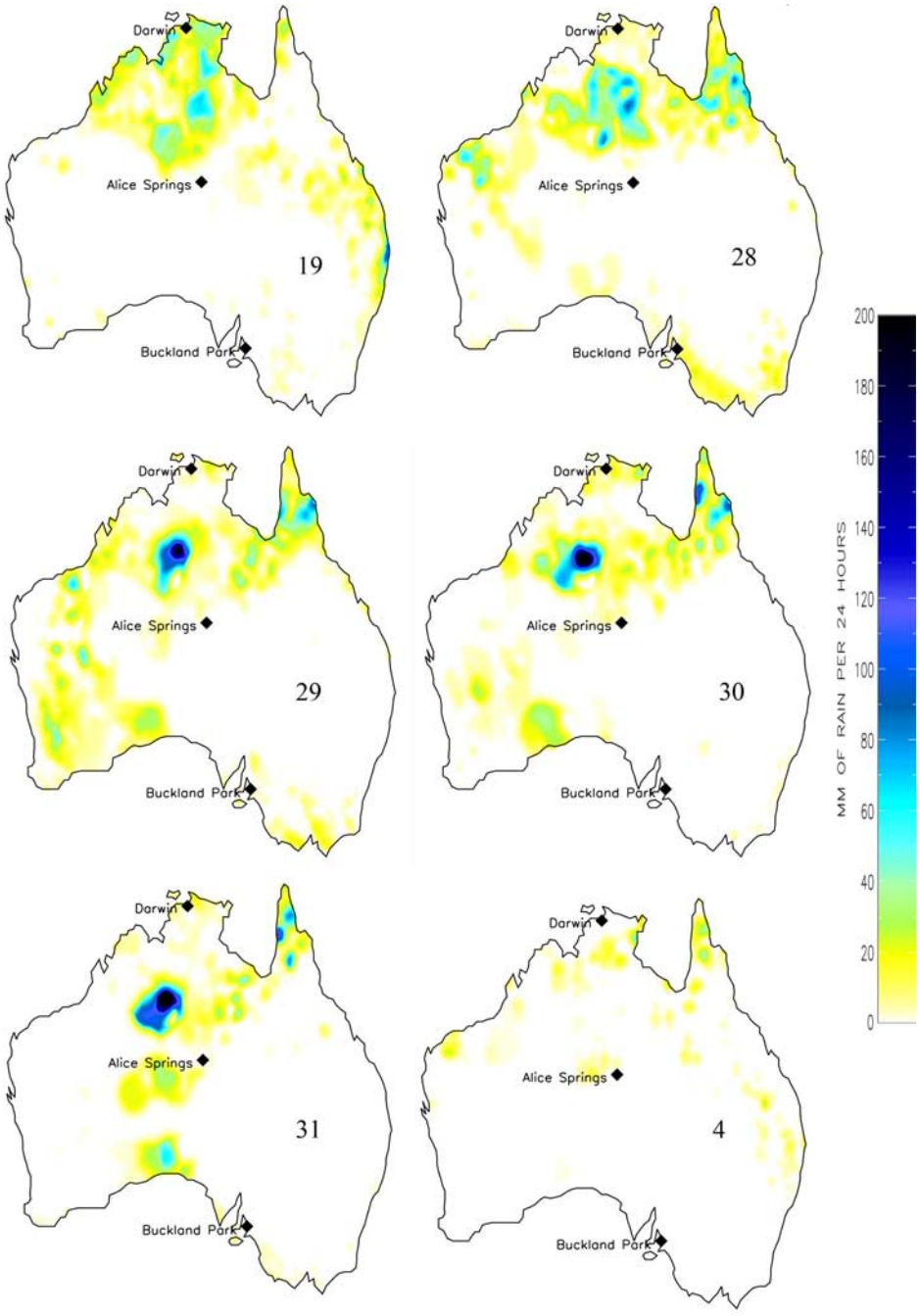

Figure 8. Rainfall maps over Australia (millimeters of rain per 24 h) for 19, 28, 29, 30, and 31 January and 4 February of 2006.

analysis will concentrate on the 31 January 2006 image event.

[55] The results of the wavelet analysis for 31 January 2006 are shown in Figures 10 and 11. Figure 10 shows the directionality of k_h (with a 180 degree uncertainty) for these waves. We only used regions where the amplitudes of the retrieved waves are above 0.48 mW/m^2-sr-cm^{-1}, which is a signal to noise (S/N) of 2. We also assume that eastward propagation with respect to the ground is favored east of a region of strong convection. The large white arrows show movement to the east, NE and SE consistent with AGWs originating near the storm center. Interestingly, over AS, where our airglow imager was observing AGWs above 80 km, the AGW phase propagation at 40 km is toward the SE. We note that there are other arrows (directions) that are not associated with the large storm. They could be due to other smaller rainfall systems. We have also not plotted results from near the edges of the AIRS image swath as they can suffer greater uncertainty in the analysis owing to wavelet wrap-around edge effects [*Alexander and Barnet*, 2007].

[56] The wavelet analysis also captures the amplitude of the dominant waves. Figure 11 shows their amplitudes with the rainfall contours superimposed. A cutoff of 0.72 mW/

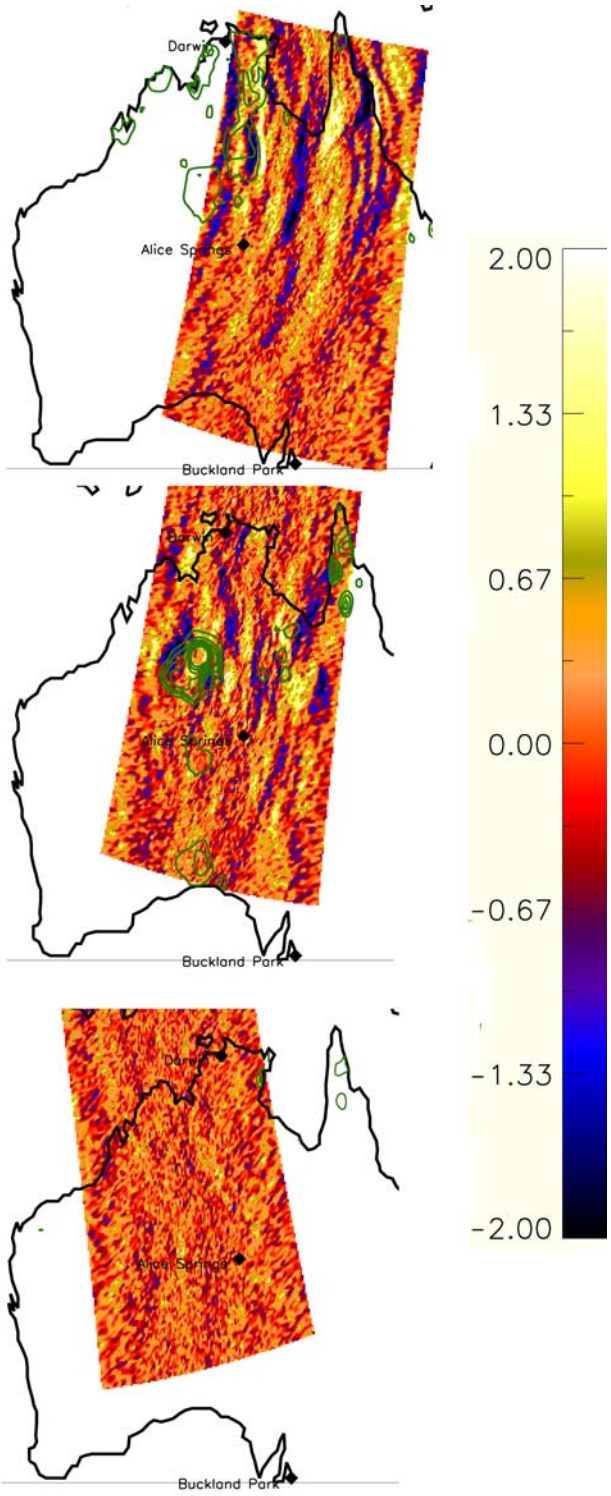

Figure 9. Images of radiance perturbations (mW/m^2-sr-cm^{-1}) from the mean calculated from AIRS data originating near 40 km altitude for (top) 1559 UT on 19 January 2006, (middle) 1623 UT on 31 January 2006, and (bottom) 0505 UT on 4 February 2006. The contours represent rainfall amounts as shown in Figure 8. The first contour represents 25 mm of rainfall over 24 h.

m^2-sr-cm^{-1}, an S/N of 3, has been used in this plot. Note that this does not show phase fronts but simply, at any location, the amplitude of the dominant AGW. The maximum amplitude is around 1.5 mW/m^2-sr-cm^{-1}, that is approximately an S/N of over 6. The associated brightness temperature amplitude is 1.6 K, and the true temperature amplitudes will be larger than this by an unknown factor that depends on the vertical wavelength of the wave. Vertical wavelength cannot be directly determined from these data. The largest perturbations occur in the region of the rainfall event, although slightly to the west.

[57] To understand the origin of these waves a ray trace was performed with a horizontal wavelength of 300 km, since the wavelet analysis revealed wavelengths between 200 and 400 km. Two observed periods were used, 120 or 25 min. The 120-min value, which was chosen to approximate the maximum AS observed periods discussed below, results in vertical wavelengths, at 40 km altitude, varying for example from about 33 km for AGWs launched due east (90 degrees east of north) to about 20 km when they are launched toward AS. These values are all well above the approximate 12 km vertical weighting function of this particular AIRS channel [*Alexander and Barnet*, 2007; *Alexander and Teitelbaum*, 2007]. The 25-min-period waves freely propagate nearly as vertical as is possible, for a 300-km λ_h AGW, up to 40 km altitude. AGWs with shorter periods encounter an evanescent region below 40 km.

[58] Figure 12 shows white lines which represent the results of the ray trace to 40 km altitude for AGWs, with varying horizontal propagation azimuths, generated at 15 km altitude at the center of the largest rainfall contour. The two arcs are for the two different observed periods that were used. For this example, AGWs would be predicted to be present at 40 km only at the positions of these two arcs. AGWs with periods between 25 and 120 min would occur between the two arcs. Note that the results of Figure 12 show only that an AGW reaches that distance from the center of the rainfall at some time. Thus the 300-km 120-min AGWs that are launched due east reach 40 km altitude in about 100 min. However, the wave launched at 30 degrees east of north reaches 40 km altitude in 140 min. Therefore the phase of the wave at 30 degrees may be quite different. Thus the line giving the locations where specified waves intersect 40 km is not a line of constant phase. This is true to a lesser extent for the shorter 25-min-period AGWs (which have fast phase speeds) as these waves even when launched from different azimuths mostly arrive at 40 km at similar times.

[59] The AIRS images show some morphological differences in their phase front orientations from this simple analysis. Because of the extended nature of the source in space and in time, and the generation of a spectrum of AGWs, interference effects between AGWs probably account for these differences. Also of interest is what generates the AGWs seen to the east of the circles in Figure 12. This will be discussed further below.

3.3. Alice Springs Results

3.3.1. Long-Period Large-Horizontal-Wavelength AGWs

[60] The ray trace analysis, using the adopted wind and temperature profiles, indicates that several-hundred-kilometer λ_h waves with observed periods of a few tens of minutes or

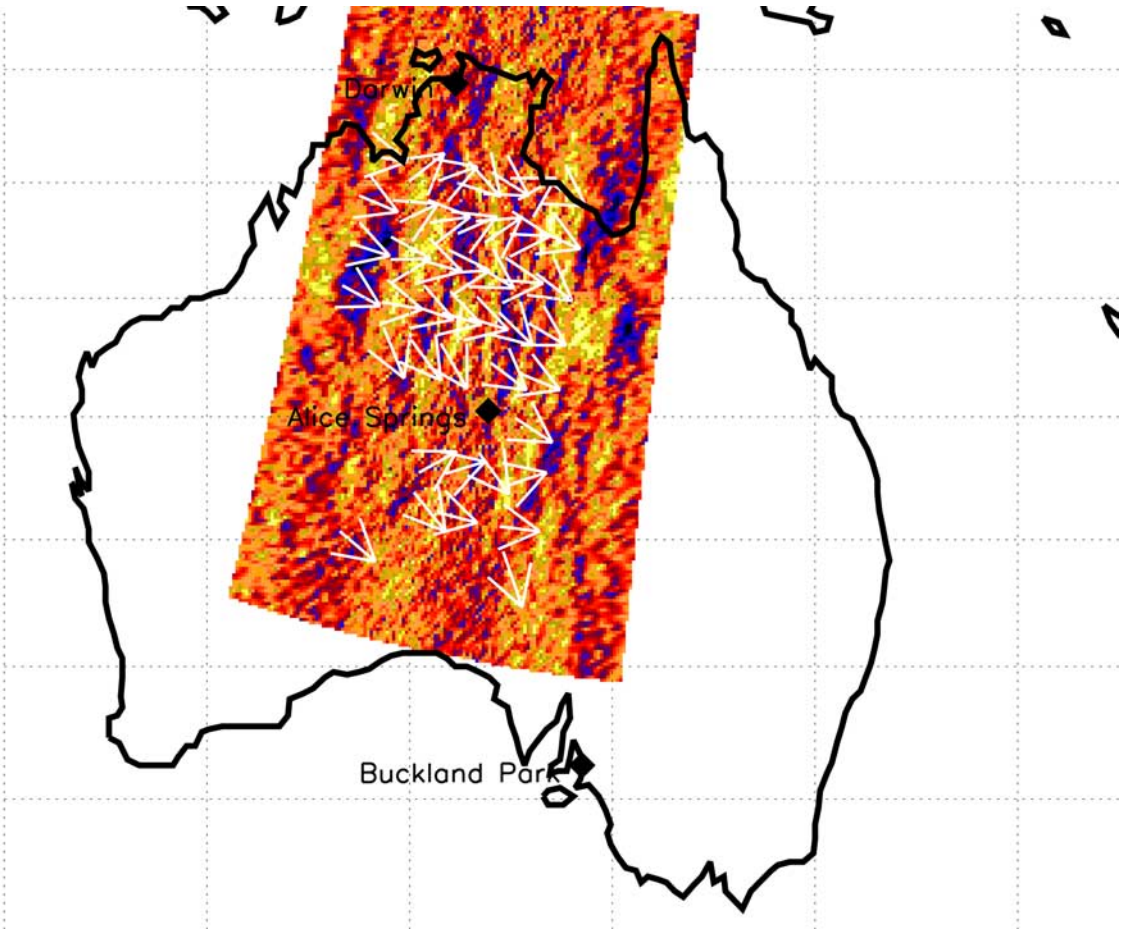

Figure 10. Same as Figure 9 (middle), without any rainfall contours, but also showing the directionality of the dominant wave from the wavelet analysis.

more should reach 85 km without encountering an evanescent region. Thus such waves should be visible in the Alice Springs (AS) airglow data. While such waves cannot be directly seen in the images because they are larger than the field of view, techniques have been developed that allow the detection of such AGWs and their approximate horizontal wavelengths [e.g., *Hecht et al.*, 1997].

[61] Figure 13 (top) shows the OHM brightness measured by the AS imager on 31 January 2006 UT. The solid line is the image average over an approximately 58 × 90 km box, while the dotted line is an average over an approximate 10 × 16 km box. There were a few images, indicated by diamonds, where clouds obscured some stars. Since the presence of clouds can affect the ability to determine OHM brightness, these data are not used in the following discussion. However, it should be noted that because clouds scatter light back into the field of view [*Gattinger et al.*, 1991] the brightness data may not necessarily be affected. Over most of the cloud-free period, what is seen are wavelike oscillations with ground-based periods on the order of 1 to 2 h. The perturbation in intensity is on the order of 10 percent. However, because the imager also obtains temperatures, we find temperature perturbations (not shown) which are between 1 and 2 percent of the mean. For the AGW around 1500–1630 UT the intensity and temperature perturbations, with respect to the mean, are approximately 8 and 1.6 percent, respectively. The ratio of these two, the Krassovsky ratio, is 5, which is in the range of the predictions of *Schubert et al.* [1991] for these AGWs.

[62] There is a difference in amplitude between the two curves in Figure 13 (top). Figure 13 (bottom) shows that this difference is on the order of 2 to 3 percent. A model was constructed where AGWs with different λ_h values were propagated through the two average boxes to determine how much the AGW amplitude was reduced. It was found that AGWs with a λ_h of about 400 km or greater show a 2 to 3 percent difference in the peak amplitude. Thus the λ_h from this analysis is close to the AIRS result suggesting that indeed similar long wavelength waves are seen at both 40 and 85 km altitudes.

[63] It is also possible to determine the propagation direction of the AGW by placing nine boxes around the image, plotting the OHM intensity in each box, and looking for time differences. This approach was used for example by *Hecht et al.* [1997]. Because there are short-scale AGWs in the images (see below), this approach is found here to be somewhat uncertain. It is clear that the 400-km λ_h AGW at around 1500 to 1600 UT is propagating north to south and west to east. However, the exact direction (i.e., how many degrees east of north) cannot be established. Nevertheless, such a direction would be consistent with an origin from the storm.

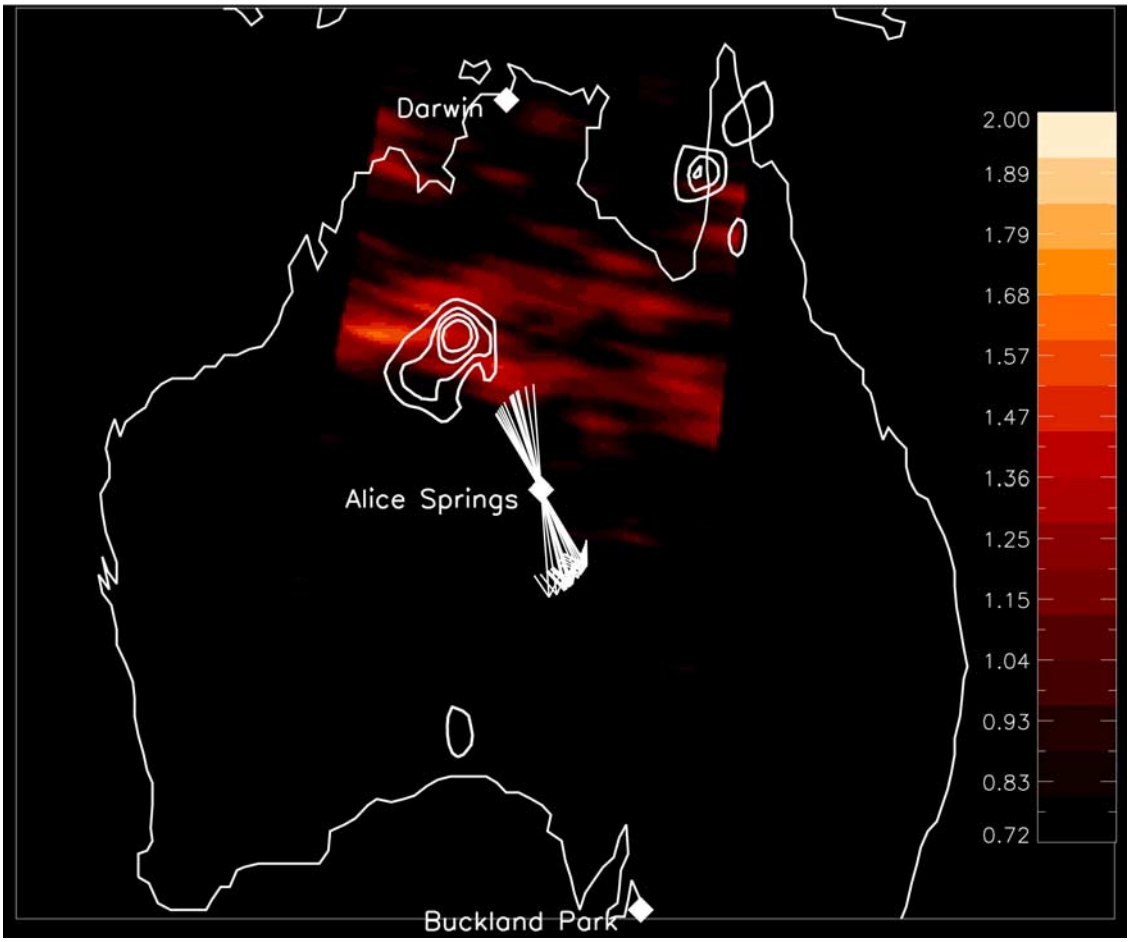

Figure 11. Wave amplitudes (mW/m^2-sr-cm^{-1}) from the wavelet analysis in Figure 9 (middle). The amplitudes have a threshold of 0.72 which represents approximately a signal 3 times the noise. The white arrows show the directionality of small-horizontal-wavelength AGWs observed by the Alice Springs imager. Here the first contour represents 50 mm of rainfall over 24 h.

[64] Ray traces were then performed, over varying horizontal propagation azimuths, for AGWS with a λ_h of 400 km and a 120-min ground-based period. These were all launched at 15 km altitude and followed until they reached 85 km altitude, the base of the airglow region. Figure 14 shows the results, which indicate that such waves would appear over the AS observing site in about 4 h. Waves generated at 1200 UT or before would reach 80 km altitude over AS at or before 1600 UT. Since the very coldest clouds presumably associated with vigorous convective rainfall were present before about 1200 UT on 31 January, the AGWs seen at AS were probably due to convection. Furthermore, on the basis of Figure 13 (top) the long period waves over AS were present prior to 1600 UT but appear to be of much lower amplitude after 1600 UT. Thus the long-period AGWs over AS may indeed be due to the convective activity that, on the basis of Figure 7, would be associated with the very cold clouds which occurred during the first half of 31 January 2006.

[65] However, since the waves observed by AIRS took about 1.5 to 2 h to reach 40 km altitude (Figure 12), those were generated after 1200 UT. Thus it is not clear if the AIRS perturbations are due to convectively generated AGWS or, as referenced earlier, AGWs generated in the outflows of this tropical cyclone-like system.

3.3.2. Short-Period Small-Horizontal-Wavelength AGWs

[66] In addition to the long-period waves, the images resolved short-period short-horizontal-wavelength AGWs that are similar to those typically seen in imagers in Australia and elsewhere [e.g., *Walterscheid et al.*, 1999; *Hecht*, 2004]. Because of the smoothing used to obtain Figure 13, these short-period waves are not resolved in these plots. However, analysis of the individual images (not shown) reveals that those observed have λ_h values from 30 to 45 km and ground-based periods of 15 to 25 min. While AGWs were imaged throughout the night observation period from 1100 to 1900 UT, they were seen in bursts, with most of the wave images being from 1100 to 1200 UT and from 1300 to 1430 UT. However, there is some uncertainty on these times as some of the periods, such as between 1210 and 1225 UT where waves were not seen, were contaminated by clouds. The propagation directions, which mostly range from 135 to 160 degrees east of north, are shown in Figure 11. The direction of phase propagation suggests that these AGWs originate from the storm region.

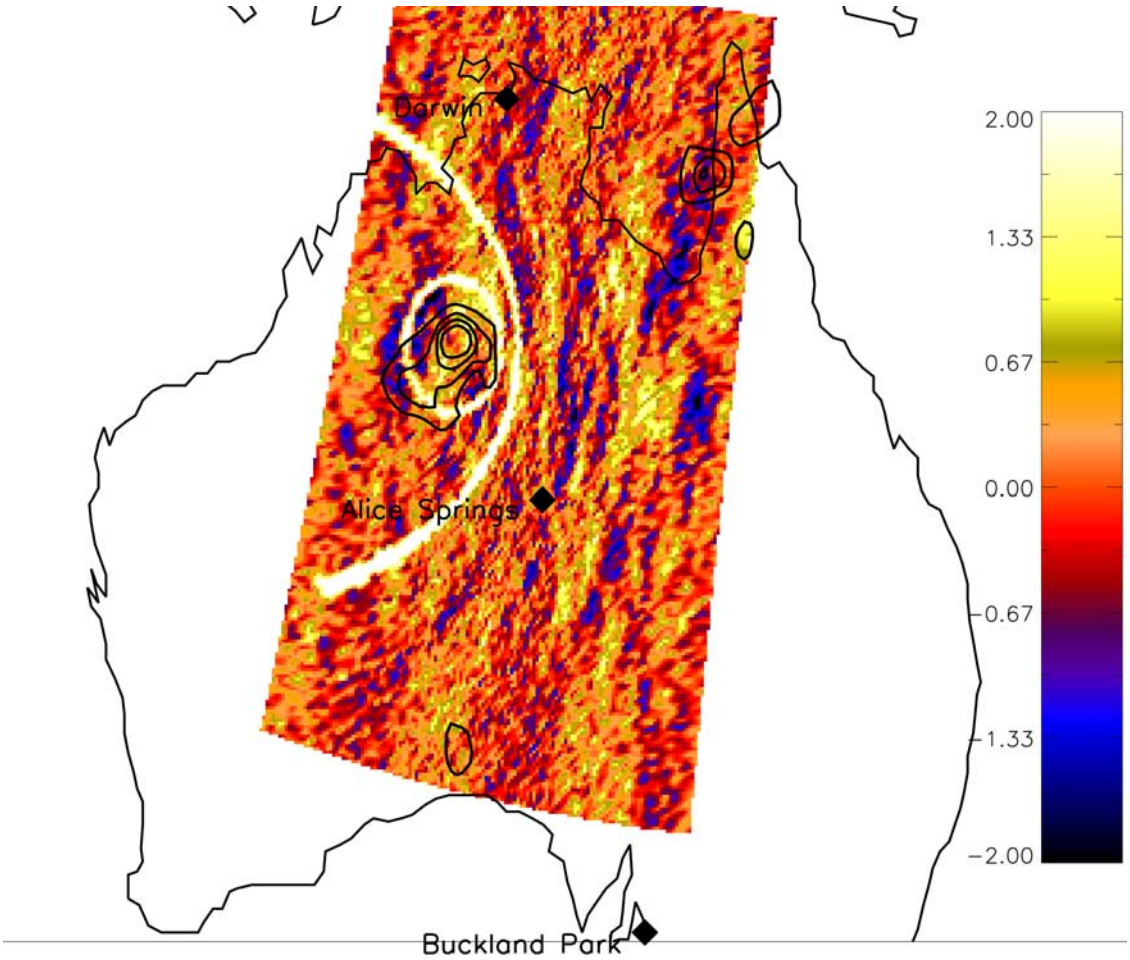

Figure 12. Same as Figure 9 (middle) but also showing the position of a 300-km λ_h 120-min ground-based period wave (outer partial circle) when it reaches 40 km altitude. For clarity in this plot the circle is only drawn where the distance to the center of the storm is less than 600 km. The inner complete circle is for the position of a 300-km λ_h 25-min ground-based period wave when it reaches 40 km altitude. Here the first contour represents 50 mm of rainfall over 24 h.

[67] To understand their origin, a ray trace was again performed. Figure 15 shows the potential problems in this approach. This shows two plots of the square of the vertical wave number, m^2, with and without winds, calculated for an AGW with a λ_h of 35 km and a ground-based period of 15 min. Between 80 and 100 km, there is a region that would be a duct or trapped region if there was an evanescent region below. However, without winds, m^2 is positive up to and above 95 km, and there is no trapped region. The solid line plots m^2 with winds for an AGW propagating 150 degrees east of north. A trapped region is formed with regions of evanescence between 60 and 80 km and around 98 km. (The lack of good winds above 98 km makes it difficult to determine how far up the evanescent region extends.) This trapped region (between 60–80 and 98 km) exists for AGWs with λ_h of 30 km and periods up to 25 min. As the λ_h increases to 45 km, the upper limit for the period is about 15 min.

[68] Consider the propagation of the AGW up to 85 km. This cannot be rigorously calculated in our approach for all propagation angles since the AGW has to tunnel through an evanescent region. However, for AGWS with a 35-km λ_h and a 15-min ground-based period, and propagating less than 38 and greater than 173 degrees east of north, m^2 is always positive and thus the trapped region vanishes given our assumed wind/temperature profile. If the λ_h is increased to 45 km, the propagation angles for freely propagating AGWs changes only slightly to less than 31 and more than 158 degrees east of north. AGWs initially propagating between these angles will see the evanescent region. Note that it is mainly the strong zonal winds that are westward below 80 km altitude in conjunction with the temperature gradients that cause the trapped region to form. Thus AGWS propagating southward and westward freely propagate.

[69] For the waves that encounter an evanescent region, we follow the procedure outlined earlier. This essentially assumes that the AGWs which encounter the evanescent region (propagation directions smaller than 174 degrees for 35-km λ_h with 15-min ground-based period AGWs) can tunnel through it in a short amount of time. To calculate the time it takes to travel to AS, we assume that once the AGWs tunnel through the evanescent region, they are trapped and then can freely propagate, bouncing between the upper and lower evanescent layers. As outlined earlier, we can then calculate how far horizontally the wave packet travels in a

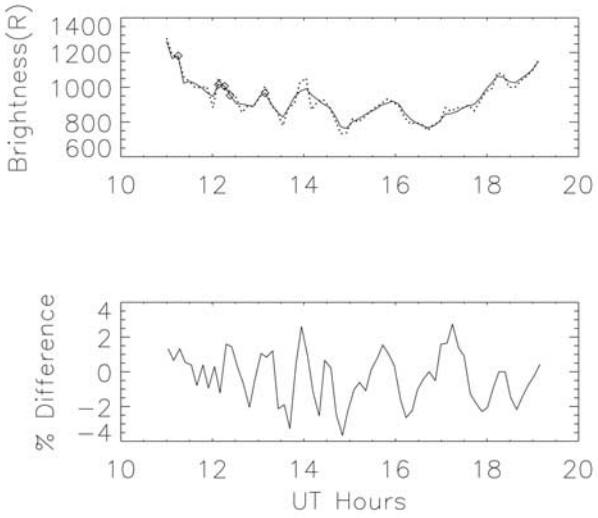

Figure 13. (top) OH brightness, in Rayleighs, measured by AS imager on 31 January 2006. The solid line is the average over approximately an 58 × 90 km box, while the dotted line is an average over a 10 × 16 km box. The diamonds indicates images where there were clouds obscuring individual stars. (bottom) Percent difference between the lines in the top plot. The statistical uncertainties are less than 1 percent of the brightness values.

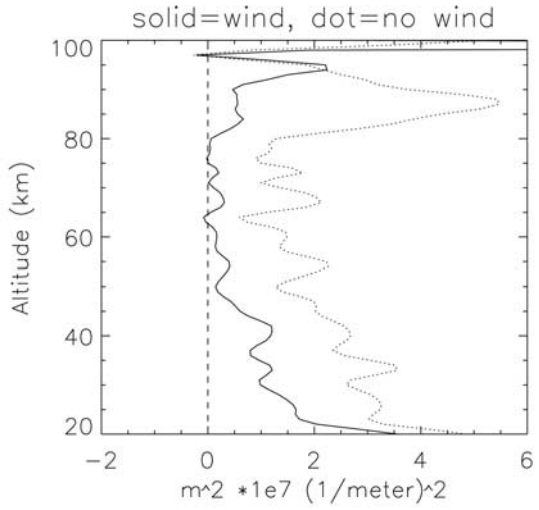

Figure 15. The m^2 from the dispersion relation for an AGW launched at an azimuth of 150 degrees east of north with a λ_h of 35 km and a ground-based period of 15 min. With winds (solid curve) and without winds (dotted curve). The evanescent regions, where m^2 are less than zero, are present for λ_h values up to about 45 km for ground-based periods of 15 min. At a λ_h of 30 km the evanescent region remains until ground-based periods reach around 25 min.

given amount of time. Thus we can calculate, for any given initial propagation direction, where an AGW will be with respect to the ground after a given amount of time.

[70] Before discussing the results of these calculations, we first comment on the vertical and horizontal propagation in the evanescent layer. The vertical group velocity was calculated from 15 to 96 km. If any evanescent region existed, the time it took to traverse this region was calculated. On the basis of Figure 15, these regions were of small vertical extent

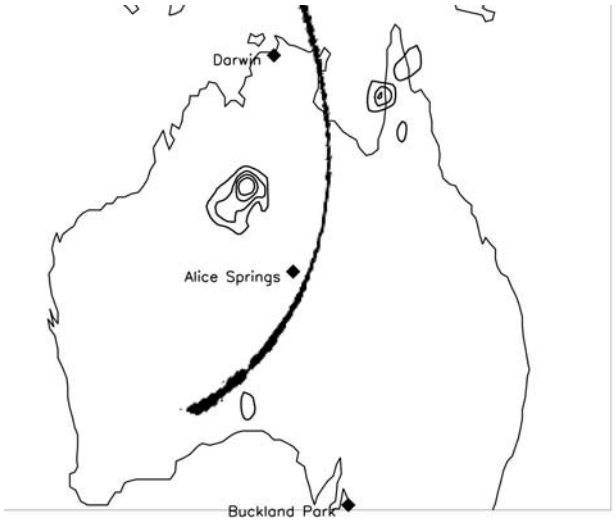

Figure 14. Similar to Figure 12 but showing a partial circle indicating the position, as determined by a ray trace, of a 400-km λ_h 120-min ground-based period AGW when it reaches 80 km altitude. For clarity, as in Figure 11, only part of the circle is shown.

(less than 1 km), mainly in the region between 60 and 80 km, and it was found that since T was above 0.95, the amount of time it took to traverse these regions was small, less than 1 min. (We note that even if the evanescent layers had a larger vertical extent, say 5 km, with the same vertical wave number, the amount of time it would take to traverse the region would be less than 5 min.) These times are small compared to the transit time it took to reach 85 km if we only calculate the times for the vertical regions where the waves are freely propagating. The calculated horizontal group velocities, with respect to the background wind, in the evanescent regions were low (below 20 m/s) and thus the resultant group velocities with respect to the ground were mainly to the west. However, even if we consider that it took 5 min to traverse vertically across the evanescent layer, the horizontal propagation distances were small (less than 30 km) and thus were ignored.

[71] Accepting the above assumption, the amount of time and horizontal distance traveled was calculated for the AGW during the vertical travel from 15 to 85 km. At that point the AGW was assumed to be trapped between 80 and 96 km. These limits were arbitrary on the basis of the available radar wind data. In fact the lower trapped region is probably below 80 km while the upper trapped region could even be above 100 km and be due to the presence of the large winds reported on by *Larsen* [2002]. Then the amount of time and horizontal distance traveled was calculated as the AGW went from 80 to 96 km. The AGW was then assumed to be reflected, and this distance was taken as that for a single reflection. The total distance traveled horizontally was the sum of the distance traveled to reach 85 km plus the distance traveled after a given number of reflections.

[72] Clearly, this is a simple approximation that also depends critically on the assumed wind profile. We found

that when we used the adopted wind profile, that is based on the average of the radar winds from BP and Darwin at 1400 UT, the AGW launched at an azimuth 150 degrees east of north for a λ_h of 45 km and a ground-based period of 15 min essentially traveled southward. In 40 min the AGWs would reach 85 km but would be displaced to the west 26 km by the time it reached 85 km altitude. The center of the rainfall is about 600 km from AS and even the edges of the main rainfall contours are about 350 km northwest (about 250 km west and north) of AS. Thus, freely propagating AGWs would not reach AS. However, even trapped waves would not reach AS as the winds would cause the wave packet to move slightly toward the west, not toward AS located to the east.

[73] However, on the basis of the variations illustrated in Figure 3, the wind direction is changing significantly during the preceding hours. At 88 km the meridional component is changing from strongly northward at 0700 UT to strongly southward at 1900 UT. Thus we used several different wind profiles to simulate the AGW launched at 150 degrees east of north. First, we simply used the average of the wind profiles at 1200 UT instead of 1400 UT. For this assumption, after 4.3 h (15 reflections) the AGU would be 155 km east and 270 km south of where it was launched, still not reaching AS. To simulate, as the TIDI data suggest, that the wind amplitudes south of Darwin decrease at a more rapid rate with respect to latitude, we produced a profile that was weighted three to one in favor of the BP winds. In that case, after 3.1 h the AGWs would travel about 300 km east and 260 km south. This AGW could have been launched at the edge of the storm (as indicated by the rainfall contours shown in Figure 11) and be seen in the AS imager. If we used wind profiles earlier than 1000 UT the AGWs would not travel far enough south to reach AS.

[74] These results are very dependent on the wind profile, which is not precisely known. Thus a more detailed analysis is not warranted. They do, however, suggest that there was a time period (1000 to 1400 UT) where favorable wind conditions existed for AGWs to be seen over AS if they were launched from the direction of the storm. The sporadic nature of the observations is probably in part due to the temporal variations in the wind profile.

4. Discussion

[75] Many of the results strongly suggest that the observed AGWs are due to the large storm. In particular three results stand out: (1) the curved wavefronts, shown in the wavelet analysis of the AIRS data, (2) the largest amplitudes in the AIRS radiance perturbations occur in the region around the largest rainfall produced by the tropical low, and (3) the propagation directions of the AGWs seen in the AS imager. However, there are a number of issues and questions that are raised by the data analysis.

4.1. Origin of Long-Wavelength AGWs in the AIRS Image Outside of the Ray Trace Area

[76] There are two regions of interest, not discussed above, where apparent AGW phase fronts are observed as can be seen in Figure 12. One is the region to the east of the 300-km λ_h 120-min ray trace circle, and a second is the region interior to the 300-km λ_h 25-min period ray trace circle. Sections 4.1.1 and 4.1.2 give some consideration as to the origin of such waves.

4.1.1. AGWs East of the 300-km λ_h 120-min-Period Ray Trace in Figure 12

[77] There are several possibilities for how AGWs could travel from the storm and still be observed by AIRS.

[78] 1. The ray trace calculations described above were done for AGWs generated over the center of the storm. Some of the AGWs seen to the east could be generated at the eastern edge of the rainfall contours. But this would not explain all the AGWs that are seen, especially those toward the eastern edge of the AIRS swath. However, as noted earlier, there was rainfall to the east of the contour region as can be seen in Figure 8. Although the time of the rainfall is not available, it is possible that the perturbations seen to the east are related to those events.

[79] 2. There could be wave dispersion as described by the following simplified analysis that illuminates aspects of what the ray trace calculates with the complete dispersion relation. Note that the equations presented on page 305 of *Lighthill* [1978] also show these aspects.

[80] For AGWs the angle of the intrinsic group velocity to the vertical, in the frame of reference of the wind (assumed to be in the k direction for this example), is easy to calculate from equation (5) in the approximation where $f \ll \omega_I \ll N$ and $m^2 \gg 1/(4H^2)$. Both of these are approximately valid for the λ_h and period of the AGWs considered in this section. The resultant equation, also discussed by *Lighthill* [1978] and *Alexander and Holton* [2004] is

$$\theta = \cos^{-1}\left((\omega_I)/N\right) = \cos^{-1}\left(\mathrm{k/m}\right) \tag{7a}$$

$$\theta = \cos^{-1}\left((\omega_o - kU)/N\right), \tag{7b}$$

where ω_o is the observed frequency. Thus, for a given horizontal wavelength, as the vertical wavelength becomes smaller (or the intrinsic period becomes larger) the AGW propagates more horizontally, and thus reaches a given altitude farther from the source. Consider two limiting cases of equation (7b), the first without winds being

$$\theta = \cos^{-1}\left(\omega_o/N\right). \tag{8}$$

Suppose the data show the longest observed period is 120 min. As the wave period changes the AGWs are dispersed with respect to θ, but the longest wave period (in this case, 120 min) sets the limit on how far east the AGW can travel with respect to the ground [e.g., *Alexander and Holton*, 2004].

[81] Now consider the other limiting case of equation (7b), where the wind velocity is large (and in the opposite direction to) the observed AGW phase velocity. The angle is now given by

$$\theta = \cos^{-1}\left(kU/N\right). \tag{9}$$

The intrinsic frequency becomes large (but still smaller than N) so that vertical wavelength is large. But in this case the angle now depends on the AGW horizontal wavelength. Therefore now the AGWs are dispersed in θ on the

basis of the horizontal wavelength. Thus for a given period, say 120 min, an 800-km λ_h AGW will travel farther east than a 700-km λ_h AGW. (But because the wave packet is advected westward by the winds, it does not travel as far east as the windless cases. This can be seen explicitly in the equations derived by *Lighthill* [1978] on page 334 and in the complete ray trace analysis using equations (6a)–(6d) performed for this work.) The transition between these two regimes occurs when the AGW phase velocity has the same magnitude as the wind velocity in the direction of the AGW. For our wind profile at 40 km altitude this occurs for a 300-km λ_h, 90-min ground-based period AGW.

[82] As the above analysis suggests, when we ray trace AGWs with a 120-min ground-based period and λ_h values above 300 km (all with vertical wavelengths larger than 30 km), we find these AGWs can travel significantly farther east. For example, an 800-km λ_h AGW travels nearly twice as far as the 300-km λ_h AGW. Furthermore, if we ray trace a 700-km λ_h AGW, it appears about 40 km closer when it reaches 40 km altitude compared to the 800-km λ_h AGW. Thus it is likely that the interpretation of the separation of the phase fronts at distances far removed from the source may not be as simple as the horizontal wavelength. This is possibly due to the different arrival times of long-horizontal-wavelength AGWs of slightly varying periods and wavelength. Alternatively, as noted above, rainfall, albeit at lower levels, also exists east of the main low (see Figure 8) and AGWS generated from convective sources associated with this rainfall will also contribute to the observations.

4.1.2. AGWs Directly Over the Tropical Low and Interior to the 300-km λ_h 25-min-Period Ray Trace in Figure 12

[83] The AGW ray trace shows that there is a zone above the tropospheric source into which AGWs, especially if their λ_h values are near 300 km, will not propagate if they originate from the center of the rainfall contours. This is represented by the interior of the inner circle of Figure 12. For AGWs to reach this region, they either are generated at the outermost rainfall contours or the waves are not internal AGWs but are internal acoustic waves. Acoustic waves have been shown to be able to travel along vertical rays [*Walterscheid et al.*, 2001], but they have not been observed to date in any of our image data and, especially at stratospheric altitudes, are apt to have very small amplitudes.

4.2. Persistence of the Trapped Region

[84] The ability of short-wavelength short-period AGWs to reach AS requires a duct or trapped region that exists for several hours. The temperature profile measured by SABER, which shows an inversion between 80 and 100 km, predisposes the atmosphere to form a trapped or ducted region. The actual formation of this region, however, depends on a suitable wind profile. We note that if we used the URAP instead of the HWM wind profile, trapping would be suppressed. Thus, as the winds change, the trapped region turns on and off, suggesting that the trapped AGWs may not be continuously present but could appear in bursts as was indeed observed. An alternative explanation, however, could be that the source is intermittent. However, the source during TWPICE was quite persistent over several days.

[85] Because winds are quite variable, it has been difficult in previous studies cited earlier to understand how ducts or trapped regions can persist for the many hours required for propagation of short-horizontal-wavelength AGWs from the source to observation region [e.g., *Hecht et al.*, 2004]. The existence of an atmosphere predisposed to forming such a region, due to a temperature inversion, may help to explain this if such inversions are shown to last for many hours. Note that a trapped region formed by a temperature inversion would allow AGWs in all directions to be trapped, not just in directions determined by large-amplitude winds. If the temperature inversion predisposed the atmosphere to form a trapped region, even small-amplitude wind variations could cause a trapped region to form. While data do show that long-lived temperature inversions, due to planetary waves, can form at mesopause altitudes [*Meriwether and Gerrard*, 2004], it is not known if such inversions form and persist at slightly higher altitudes, above the mesopause.

[86] For this event the presence of the quasi 2-day wave (QTDW) controls the major portion of the wind profile, and its long period would be consistent with favorable ducting or trapped conditions existing for many hours. If the existence of a temperature inversion is linked to the presence of planetary waves, and thus the inversions are long-lived, then this might explain the formation of persistent ducts, necessary for the transport of short-wavelength AGWs.

[87] In these observations the QTDW may have an effect on the temperature profile. SABER data, at night, over Australia were looked at for several days preceding 31 January. A temperature inversion from 80 to 100 km was present around 1400 UT on 31 and 29 January but was absent at this time on 30 and 28 January. The airglow data were also examined for clear periods on those four nights. Brighter and more frequent AGWs occurred on 29 and 31 January as compared to the nights of 28 and 30 January. However, in order to determine if such an association is real, more data need to be examined. Thus it would be useful to examine the SABER data on a climatological basis to determine the frequency of occurrence of such inversions and whether they are linked to observations of AGWs in imager results.

5. Conclusions

[88] The data sets described here (AIRS and airglow images) and obtained on 31 January 2006 over central Australia show strong evidence for AGWs that presumably originate in the troposphere, owing to processes associated with the large rainfall of an intense tropical low, and then propagate to the stratosphere and to the upper mesosphere. Cloud temperature data show that this low formed into a well-defined tropical cyclone-like cloud field by 31 January 2006, and during the period of 26 to 31 January 2006, there was probably considerable convective as well as stratiform rainfall. Convective rainfall is known to be associated with the formation of AGWs [*Vadas et al.*, 2009]. While, after about 1200 UT on 31 January, stratiform rainfall probably dominated, an additional source for AGWS may be associated with the upper-level outflow region of tropical cyclones that are close to inertially neutral.

[89] By ray tracing the AGWs from the troposphere, it is shown that 300/400-km-horizontal-wavelength 120-min

ground-based period AGWs could be responsible for some of the perturbations seen in the AIRS data at 40 km altitude, and also seen in OHM airglow brightness data over AS near 85 km altitude on 31 January 2006. The AGWs seen in the AIRS data probably originated after 1200 UT on 31 January 2006 and thus may be generated by convection or by processes associated with the outflow from cyclones. The AGWs seen in the AS data originated at and before 1200 UT and therefore are more probably due to convection.

[90] The AS airglow data also show 30- to 45-km horizontal wavelength, 15- to 25-min ground-based period AGWs being present for many time intervals from 1100 to 2000 UT on 31 January 2006. Ray tracing shows those waves could not reach the 80 to 90 km altitude region over AS directly; those waves must have been trapped or ducted. These waves take several hours to reach the mesopause region over AS, and they were probably mostly launched before 1200 UT on 31 January 2006. Thus these AGWs were probably generated by convection.

[91] The SABER data show that for those short-wavelength AGWs a trapped region is almost formed by the temperature profile, which shows a temperature inversion. The inclusion of the wind profile obtained from available data and models shows that a trapped region does form. In order for the AGWs to reach AS, however, the trapped region must exist for many hours. However, since the winds are dominated by a QTDW, and the temperature profile, from SABER, shows an inversion which extends for many vertical kilometers, such a long-lived region is plausible.

[92] The SABER data were also examined to see if inversions were present on previous nights. It was found that an inversion was found on 29 and 31 January. The AS image data showed that brighter and more frequent waves were seen on those nights. This suggests a connection between the presence of long-period waves, such as the QTDW and other planetary waves, and the possibility of trapped AGWs being observed in airglow images over Australia.

[93] **Acknowledgments.** Thanks go to Peter Strickland and Jeremy Ward for the considerable help at Alice Springs. Elizabeth Ebert of the Centre for Australian Weather at the Bureau of Meteorology in Melbourne, Australia, provided the rainfall data. The Aerospace Corporation's results could not have been obtained without the invaluable help given by Kirk Crawford in all aspects of this project. J.H.H., R.L.W., and L.J.G. were supported by NSF grants ATM-0737557 and ATM-0436516 and by NASA grant NAG5-13025. M.J.A. was supported by the NASA program Earth System Science Research using data and products from TERRA, AQUA, and ACRIM Satellites, contracts NNH04CC54C and NNH08AH43I. R.A.V. acknowledges support from Australian Research Council grant DP0558361. The authors acknowledge the SABER science team for their role in developing the scientific algorithms for the SABER temperatures. W.R.S. was supported in part by NASA grant NAG5 5049. P.T.M. acknowledges the support of the Department of Energy Atmospheric Radiation Measurement Program. TWP-ICE was supported under the auspices of the U.S. Department of Energy ARM Program, the ARM Uninhabited Aerospace Vehicle (UAV) Program, NASA CloudSat, the UK Natural Environment Research Council (NERC) grant NE/C512688/1, the NERC Airborne Remote Sensing Facility, the Australian National Marine Research Facility, the Australian Bureau of Meteorology, and the Kyoto University Active Geosphere Investigation (KAGI) for the 21st century COE program. Centre for Australian Weather and Climate Research is a partnership between the Australian Bureau of Meteorology and CSIRO. Vaisala generously donated the radiosonde base stations. The Charles Darwin University, Darwin RAAF Base, and the Tiwi Island Land Council all made extensive facilities available to the experiment. The initial version of the wavelet software was provided by C. Torrence and G. Compo and is available at http://paos.colorado.edu/research/wavelets/.

References

Alexander, M. J., and C. Barnet (2007), Using satellite observations to constrain parameterizations of gravity wave effects for global models, *J. Atmos. Sci.*, *64*, 1652–1665.

Alexander, M. J., and J. R. Holton (2004), On the spectrum of vertically propagating gravity waves generated by a transient heat source, *Atmos. Chem. Phys.*, *4*, 923–932.

Alexander, M. J., and H. Teitelbaum (2007), Observation and analysis of a large amplitude mountain wave event over the Antarctic Peninsula, *J. Geophys. Res.*, *112*, D21103, doi:10.1029/2006JD008368.

Alexander, M. J., P. T. May, and J. H. Beres (2004), Gravity waves generated by convection in the Darwin area during DAWEX, *J. Geophys. Res.*, *109*, D20S04, doi:10.1029/2004JD004729.

Aumann, H. H., et al. (2003), AIRS/AMSU/HSB on the Aqua mission: Design, science objectives, data products, and processing systems, *IEEE Trans. Geosci. Remote Sens.*, *41*, 253–264.

Dewan, E. M., R. H. Picard, R. R. O'Neill, H. A. Gardiner, J. Gibson, J. D. Mill, E. Richards, M. Kendra, and W. O. Gallery (1998), MSX satellite observations of thunderstorm-generated gravity waves in mid-wave infrared images of the upper stratosphere, *Geophys. Res. Lett.*, *25*(7), 939–942.

Eckermann, S. D., and C. J. Marks (1996), An idealized ray model of gravity wave-tidal interactions, *J. Geophys. Res.*, *101*(D16), 21,195–21,212.

Ejiri, M. K., K. Shiokawa, T. Ogawa, K. Igarashi, T. Nakamura, and T. Tsuda (2003), Statistical study of short-period gravity waves in OH and OI nightglow images at two separated sites, *J. Geophys. Res.*, *108*(D21), 4679, doi:10.1029/2002JD002795.

Fritts, D. C., and M. J. Alexander (2003), Gravity wave dynamics and effects in the middle atmosphere, *Rev. Geophys.*, *41*(1), 1003, doi:10.1029/2001RG000106.

Gattinger, R. L., A. V. Jones, J. H. Hecht, D. J. Strickland, and J. Kelly (1991), Comparison of ground-based optical observations of N_2 second positive to N_2^+ first negative emission ratios with electron precipitation energies inferred from the Sondre Stromfjord radar, *J. Geophys. Res.*, *96*(A7), 11,341–11,351.

Gossard, E. E., and W. H. Hooke (1975), *Waves in the Atmosphere, Atmospheric Infrasound and Gravity Waves: Their Generation and Propagation*, 456 pp., Elsevier, Amsterdam.

Hamilton, K., R. A. Vincent, and P. T. May (2004), The DAWEX field campaign to study gravity wave generation and propagation, *J. Geophys. Res.*, *109*, D20S01, doi:10.1029/2003JD004393.

Hecht, J. H. (2004), Instability layers and airglow imaging, *Rev. Geophys.*, *42*, RG1001, doi:10.1029/2003RG000131.

Hecht, J. H., R. L. Walterscheid, and M. N. Ross (1994), First measurements of the two-dimensional horizontal wavenumber spectrum from CCD images of the nightglow, *J. Geophys. Res.*, *99*(A6), 11,449–11,460.

Hecht, J. H., R. L. Walterscheid, D. C. Fritts, J. R. Isler, D. C. Senft, C. S. Gardner, and S. J. Franke (1997), Wave breaking signatures in OH airglow and sodium densities and temperatures: 1. Airglow imaging, Na lidar, and MF radar observations, *J. Geophys. Res.*, *102*(D6), 6655–6668.

Hecht, J. H., R. L. Walterscheid, M. P. Hickey, and S. J. Franke (2001), Climatology and modeling of quasi-monochromatic atmospheric gravity waves observed over Urbana, Illinois, *J. Geophys. Res.*, *106*(D6), 5181–5196.

Hecht, J. H., S. Kovalam, P. T. May, G. Mills, R. A. Vincent, R. L. Walterscheid, and J. Woithe (2004), Airglow imager observations of atmospheric gravity waves at Alice Springs and Adelaide, Australia during the Darwin Area Wave Experiment (DAWEX), *J. Geophys. Res.*, *109*, D20S05, doi:10.1029/2004JD004697.

Hedin, A. E., et al. (1996), Empirical wind model for the upper, middle and lower atmosphere, *J. Atmos. Terr. Phys.*, *58*, 1421–1427, doi:10.1016/0021-9169(95)00122-0.

Holdsworth, D. A., and I. M. Reid (2004), The Buckland Park MF radar: Routine observation scheme and velocity comparisons, *Ann. Geophys.*, *22*(11), 3815–3828.

Holdsworth, D. A., I. M. Reid, and M. A. Cervera (2004), Buckland Park all-sky interferometric meteor radar, *Radio Sci.*, *39*, RS5009, doi:10.1029/2003RS003014.

Houze, R. A., Jr. (1993), *Cloud Dynamics*, 573 pp., Academic Press, San Diego, Calif.

Jones, W. L. (1969), Ray tracing for internal gravity waves, *J. Geophys. Res.*, *74*, 2028–2033.

Keenan, T. D., and R. E. Carbone (1992), A preliminary morphology of precipitation systems in tropical northern Australia, *Q. J. R. Meteorol. Soc.*, *118*, 283–326.

Killeen, T. L., et al. (1999), TIMED Doppler Interferometer (TIDI), in *SPIE Conference on Optical Spectroscopic Techniques and Instrumentation for Atmospheric and Space Research III, SPIE 3756*, pp. 289–301, SPIE–Int. Soc. for Opt. Eng., Denver, Colo.

Larsen, M. F. (2002), Winds and shears in the mesosphere and lower thermosphere: Results from four decades of chemical release wind measurements, *J. Geophys. Res.*, *107*(A8), 1215, doi:10.1029/2001JA000218.

Lighthill, J. (1978), *Waves in Fluids*, 504 pp., Cambridge Univ. Press, Cambridge, U. K.

Marks, C. J., and S. D. Eckermann (1995), A three-dimensional nonhydrodynamic ray-tracing model for gravity waves: Formulation and preliminary results for the middle atmosphere, *J. Atmos Sci.*, *52*, 1959–1984.

May, P. T., G. J. Holland, and W. L. Ecklund (1994), Wind profiler observations of tropical storm Flo at Saipan, *Weather Forecast.*, *9*, 410–426.

May, P. T., J. H. Mather, G. Vaughan, C. Jakob, G. M. McFarquhar, K. N. Bower, and G. G. Mace (2008), The Tropical Warm Pool International Cloud Experiment, *Bull. Am. Meteorol. Soc.*, *89*, 629–645, doi:10.1175/BAMS-89-5-629.

Meriwether, J. W., and A. J. Gerrard (2004), Mesosphere inversion layers and stratosphere temperature enhancements, *Rev. Geophys.*, *42*, RG3003, doi:10.1029/2003RG000133.

Mertens, C. J., M. G. Mlynczak, M. Löpez-Puertas, P. P. Wintersteiner, R. H. Picard, J. R. Winick, L. L. Gordley, and J. M. Russell III (2001), Retrieval of mesospheric and lower thermospheric kinetic temperature from measurements of CO_2 15 μm Earth limb emission under non-LTE conditions, *Geophys. Res. Lett.*, *28*(7), 1391–1394.

Nakamura, T., A. Higashikawa, T. Tsuda, and Y. Matsushita (1999), Seasonal variations of gravity wave structures in OH airglow with a CCD imager at Shigaraki, *Earth Planets Space*, *51*, 897–906.

Nakamura, T., T. Aono, T. Tsuda, A. G. Admiranto, E. Achmad, and Suranto (2003), Mesospheric gravity waves over a tropical convective region observed by OH airglow imaging in Indonesia, *Geophys. Res. Lett.*, *30*(17), 1882, doi:10.1029/2003GL017619.

Niciejewski, R., Q. Wu, W. Skinner, D. Gell, M. Cooper, A. Marshall, T. Killeen, S. Solomon, and D. Ortland (2006), TIMED Doppler Interferometer on the Thermosphere Ionosphere Mesosphere Energetics and Dynamics satellite: Data product overview, *J. Geophys. Res.*, *111*, A11S90, doi:10.1029/2005JA011513.

Pautet, P.-D., M. J. Taylor, A. Z. Liu, and G. R. Swenson (2005), Climatology of short-period gravity waves observed over northern Australia during the Darwin Area Wave Experiment (DAWEX) and their dominant source regions, *J. Geophys. Res.*, *110*, D03S90, doi:10.1029/2004JD004954.

Press, W. H., S. A. Teukolsky, W. T. Vettering, and B. P. Flannery (1993), *Numerical Recipes: The Art of Scientific Computing*, 2nd ed., 1020 pp., Cambridge Univ. Press, Cambridge, U. K.

Remsberg, E. E., et al. (2008), Assessment of the quality of the Version 1.07 temperature-versus-pressure profiles of the middle atmosphere from TIMED/SABER, *J. Geophys. Res.*, *113*, D17101, doi:10.1029/2008JD010013.

Russell, J. M., III, M. G. Mlynczak, L. L. Gordley, and J. Tansock (1999), An overview of the SABER experiment and preliminary calibration results, *Proc. SPIE, Int. Soc. Opt. Eng.*, *3756*, 277–288.

Schubert, G., R. L. Walterscheid, and M. P. Hickey (1991), Gravity wave-driven fluctuations in OH nightglow from an extended, dissipative emission region, *J. Geophys. Res.*, *96*(A8), 13,869–13,880.

Sentman, D. D., E. M. Wescott, R. H. Picard, J. R. Winick, H. C. Stenbaek-Nielsen, E. M. Dewan, D. R. Moudry, F. T. Sao Sabbas, M. J. Heavner, and J. Morrill (2003), Simultaneous observations of mesospheric gravity waves and sprites generated by a midwestern thunderstorm, *J. Atmos. Sol. Terr. Phys.*, *65*, 537–550.

Skinner, W. R., et al. (2003), Operation performance of the TIMED Doppler Interferometer (TIDI), in *SPIE Conference on Optical Spectroscopic Techniques and Instrumentation for Atmospheric and Space Research V, SPIE 5157*, edited by A. M. Larar et al., pp. 47–57, SPIE–Int. Soc. for Opt. Eng., San Diego, Calif.

Snively, J. B., and V. P. Pasko (2008), Excitation of ducted gravity waves in the lower thermosphere by tropospheric sources, *J. Geophys. Res.*, *113*, A06303, doi:10.1029/2007JA012693.

Suzuki, S., K. Shiokawa, Y. Otsuka, T. Ogawa, and P. Wilkinson (2004), Statistical characteristics of gravity waves observed by an all-sky imager at Darwin, Australia, *J. Geophys. Res.*, *109*, D20S07, doi:10.1029/2003JD004336.

Swinbank, R., and D. A. Ortland (2003), Compilation of wind data for the UARS reference atmosphere project, *J. Geophys. Res.*, *108*(D19), 4615, doi:10.1029/2002JD003135.

Taylor, M. J., and M. A. Hapgood (1988), Identification of a thunderstorm as a source of short period gravity waves in the upper atmospheric nightglow emissions, *Planet. Space Sci.*, *36*, 975–985.

Torrance, C. T., and G. P. Compo (1998), A practical guide to wavelet analysis, *Bull. Am. Meteorol. Soc.*, *71*, 61–78.

Vadas, S. L., and D. C. Fritts (2006), Thermospheric responses to gravity waves: Influences of increasing viscosity and thermal diffusivity, *J. Geophys. Res.*, *110*, D15103, doi:10.1029/2004JD005574.

Vadas, S., M. J. Taylor, D. Pautet, P. A. Stamus, D. C. Fritts, F. Sao Sabbas, and V. Thiago (2009), Convection: The likely source of the medium-scale gravity waves observed in the OH airglow layer near Brasilia, Brazil, during the SpreadFEx Campaign, *Ann. Geophys.*, *27*, 231–259.

Walterscheid, R. L., and J. H. Hecht (2003), A reexamination of evanescent acoustic-gravity waves: Special properties and aeronomical significance, *J. Geophys. Res.*, *108*(D11), 4340, doi:10.1029/2002JD002421.

Walterscheid, R. L., J. H. Hecht, R. A. Vincent, I. M. Reid, J. Woithe, and M. P. Hickey (1999), Analysis and interpretation of airglow and radar observations of quasi-monochromatic gravity waves in the upper mesosphere and lower thermosphere over Adelaide, Australia (35°S, 138°E), *J. Atmos. Sol. Terr. Phys.*, *61*, 461–468.

Walterscheid, R. L., G. Schubert, and D. G. Brinkman (2001), Small-scale gravity waves in the upper mesosphere and lower thermosphere generated by deep tropical convection, *J. Geophys. Res.*, *106*(D23), 31,825–31,832, doi:10.1029/2000JD000131.

M. J. Alexander, Colorado Research Associates Division, NorthWest Research Associates, 3380 Mitchell Lane, Boulder, CO 80301, USA. (alexand@cora.nwra.com)

L. J. Gelinas, J. H. Hecht, and R. L. Walterscheid, Space Sciences Department, Aerospace Corporation, P.O. Box 92957, Mail Stop M2-260, Los Angeles, CA 90009, USA. (lynette.gelinas@aero.org; james.hecht@aero.org; richard.walterscheid@aero.org)

A. D. MacKinnon, R. A. Vincent, and J. M. Woithe, Department of Physics and Mathematical Physics, University of Adelaide, Adelaide, SA 5005, Australia. (andrew.mackinnon@physics.adelaide.edu.au; robert.vincent@physics.adelaide.edu.au; jwoithe@physics.adelaide.edu.au)

P. T. May, Centre for Australian Weather and Climate Research, Melbourne, Vic 3001, Australia. (pmay@bom.gov.au)

M. G. Mlynczak, Climate Science Branch, NASA Langley Research Center, Hampton, VA 23681-2199, USA. (martin.g.mlynczak@nasa.gov)

J. M. Russell III, Center for Atmospheric Sciences, Hampton University, 23 Tyler Street, Hampton, VA 23668, USA. (james.russell@hamptonu.edu)

W. R. Skinner, Department of Atmospheric, Oceanic and Space Sciences, University of Michigan, 2455 Hayward Street, Room 2517B, Ann Arbor, MI 48109-2143, USA. (wskinner@umich.edu)